Chronic depletion of subcellular NAD pools reveals their interconnectivity and a buffering function of mitochondria

Magali VanLinden
University of Bergen
Lena Høyland
University of Bergen https://orcid.org/0000-0002-7189-780X
Jörn Dietze
UiT The Arctic University of Norway
Ingvill Tolås
University of Bergen https://orcid.org/0000-0002-1162-4930
Lars Sverkeli
University of Bergen
Marc Niere
University of Bergen
Camila Cimadamore-Werthein
University of Cambridge
Barbara van den Hoeven
University of Bergen
Øyvind Strømland
University of Bergen
Roland Sauter
UiT The Arctic University of Norway https://orcid.org/0000-0002-7655-7281
Christian Dölle
University of Bergen https://orcid.org/0000-0003-2427-8130
Cedric Davidsen
Haukeland University Hospital
Ina Pettersen
University of Bergen
Karl Johan Tronstad
University of Bergen https://orcid.org/0000-0003-3496-3123
Roberto Megias Perez
University of Bergen https://orcid.org/0000-0002-1420-1845
Svein Mjøs

University of Bergen https://orcid.org/0000-0002-5948-7373
Mikhail Makarov
University of South Alabama
Marie Migaud
University of South Alabama
Ines Heiland
UiT The Arctic University of Norway
Mathias Ziegler (Mathias.Ziegler@uib.no)
University of Bergen https://orcid.org/0000-0001-6961-2396

Article

Keywords: subcellular NAD pools, NAD-dependent processes, depletion, poly-ADP-ribose-polymerases (PARPs)

Posted Date: February 4th, 2021

DOI: https://doi.org/10.21203/rs.3.rs-116850/v1

Chronic depletion of subcellular NAD pools reveals their interconnectivity and a buffering function of mitochondria

Magali R. VanLinden[1] , Lena E. Høyland[1], Jörn Dietze[2], Ingvill Tolås[3], Lars J. Sverkeli[1,3], Marc Niere[1], Camila Cimadamore-Werthein[4], Barbara van den Hoeven[1], Øyvind Strømland[1], Roland Sauter[2], Christian Dölle[5,6] , Cedric Davidsen[7], Ina K.N. Pettersen[1], Karl J. Tronstad[1], Roberto Megias Perez[1], Svein A. Mjøs[8], Mikhail V. Makarov[9], Marie E. Migaud[9], Ines Heiland[2,6,*] and Mathias Ziegler[1,10,*]

[1] Department of Biomedicine, University of Bergen, Bergen, 5009, Norway
[2] Department of Arctic and Marine Biology, UiT The Arctic University of Norway, Tromsø, 9037 Norway
[3] Department of Biological Sciences, University of Bergen, Bergen, 5020, Norway
[4] MRC Mitochondrial Biology Unit, University of Cambridge, Cambridge Biomedical Campus, Cambridge, CB2 0XY, UK
[5] Neuro-SysMed, Department of Neurology, Haukeland University Hospital, Bergen, 5021, Norway
[6] Department of Clinical Medicine, University of Bergen, Bergen, 5020, Norway.
[7] Department of Heart Disease, Haukeland University Hospital, Bergen, 5021, Norway
[8] Department of Chemistry, University of Bergen, Bergen, 5020, Norway
[9] Mitchell Cancer Institute, University of South Alabama, Mobile, AL 36604, USA
[10] Lead contact, Institute of Biomedicine, University of Bergen, Postbox7804, 5020 Bergen, Norway, Phone: +47 55 58 45 91, Email: Mathias.Ziegler@uib.no.
[*] These authors contributed equally.

Abstract

The coenzyme NAD is consumed by signaling enzymes including poly-ADP-ribose-polymerases (PARPs) and sirtuins. Understanding the mechanisms of aging-associated NAD decline and how cells cope with decreased NAD concentrations requires model systems reflecting chronic NAD deficiency. To evoke compartment-specific over-consumption of NAD, we have engineered cell lines expressing PARP activity in mitochondria, the cytosol, endoplasmic reticulum, or peroxisomes. Irrespective of the compartment targeted, total cellular NAD concentrations declined by ~40%. Isotope-tracer flux measurements and mathematical modeling showed that the lowered NAD concentration limits total NAD consumption kinetically. Moreover, NAD biosynthesis rate and capacity remained unchanged, thereby also precluding an increase of total NAD turnover. The chronic NAD deficiency was surprisingly well tolerated unless the mitochondria were targeted. Oxidative phosphorylation and glycolysis were little affected by NAD over-consumption in the other compartments. Likewise, peroxisomal NAD over-consumption was balanced by mitochondrial NAD decrease to maintain beta-oxidation of very long chain fatty acids in peroxisomes. We propose that subcellular NAD pools are interconnected, with mitochondria acting as a rheostat to facilitate NAD-dependent processes in organelles with excessive consumption.

Introduction

Among the most versatile and widely represented biomolecules in all living cells is NAD. As a redox factor, it participates in most, if not all branches of metabolism [1]. In metabolic reactions, NAD serves as electron carrier being interconverted between its oxidized (NAD^+) and reduced (NADH) form [2-5]. In addition to its redox functions, a variety of signaling processes require the cleavage of NAD^+. Most prominently, NAD^+ is the substrate of ADP-ribosyltransferases (ARTs), sirtuins and ADP-ribosylcyclases such as CD38 and SARM1 [6-10]. The most thoroughly studied ART, poly-ADP-ribose polymerase 1 (PARP1), modifies itself and other proteins with polymers of ADP-ribose derived from cleavage of NAD^+ accompanied by the release of nicotinamide (Nam). PARP1 resides in the nucleus and its function is primarily associated with DNA damage detection and facilitation of the DNA repair process [11-15]. Sirtuins, which reside in the nucleus, cytosol and mitochondria, remove acyl groups from proteins by cleaving NAD^+ and transferring the acyl group onto the ADP-ribose moiety, thus generating O-acyl-ADP-ribose and Nam [10,16,17]. The functions of sirtuins range from epigenetic and transcriptional regulation

to direct modulation of the activity of metabolic enzymes [18-24]. ADP-ribosyl cyclases generate the calcium messengers cyclic ADP-ribose and NAADP from NAD^+ and $NADP^+$, respectively, reactions which are also accompanied by the release of Nam [25-27].

This remarkable array of NAD^+-consuming processes needs to be counterbalanced by NAD^+ biosynthesis. The major route of NAD^+ synthesis in mammals recycles Nam produced in the signaling reactions [28,29]. A limited amount of NAD is also generated from quinolinic acid, a product of tryptophan degradation, and from nicotinic acid [30-32]. Nam is converted to nicotinamide mononucleotide (NMN) by nicotinamide phosphoribosyl transferase, NAMPT [28,33,34], an enzyme that has evolved an unusually high affinity to Nam to prevent excessive loss of the precursor [35]. NMN is also produced by nicotinamide riboside kinases (NRKs) using the nucleoside form of nicotinamide (NR) as substrate [36]. To form NAD^+, NMN combines with the adenylyl moiety of ATP in a reaction catalyzed by NMN adenylyltransferases (NMNATs) [37]. There are three NMNAT isoforms in mammals that provide the only obvious indication of compartment-specific NAD^+ biosynthesis, as they have been localized to the nucleus (NMNAT1), the Golgi complex, facing the cytosol (NMNAT2) and the mitochondrial matrix (NMNAT3) [38].

Compartment-specific NAD homeostasis has been highlighted in recent studies as an important determinant of physiological processes such as adipocyte differentiation, neuronal cell survival, metabolic regulation of transcription, and electron transport chain activity [39-44]. The mitochondrial NAD pool has been shown to be of particular importance to protect cells in stress situations [45,46]. However, the way in which mitochondrial NAD might contribute to counteract stress originating from other cellular components is not known. It appears that the mitochondrial NAD pool has a certain degree of autonomy, as indicated by these observations, but also by the presence of NMNAT3 within this organelle [38]. Nevertheless, how this pool is

generated and maintained is still a matter of debate and investigation. Previously, evidence has been presented suggesting the uptake of NMN or NAD^+ into the organelles [41,47,48]. Import of NMN appears plausible, given the presence of NMNAT3 in the matrix, capable of using it to form NAD^+. However, the recent discovery of SLC25A51, or MCART1, as a mammalian mitochondrial NAD^+ transporter has established the molecular basis for the major route of generation of the mitochondrial NAD^+ pool [49,50]. Additionally, NMNAT3 has been demonstrated to be dispensable in mice, further suggesting that this enzyme is not essential for mitochondrial NAD^+ synthesis [51].

Besides the nucleus, cytosol and mitochondria, NAD^+ has also been detected in other subcellular compartments including the peroxisomes and the endoplasmic reticulum (ER) [52,53]. For peroxisomes, a carrier has been described as a possible candidate [54], whereas the route of entry of NAD into the ER remains unknown. A fundamental question therefore relates to the connectivity between the individual NAD pools. To what extent are they autonomous or independent? That is, does local consumption of NAD^+ remain a local affair or does excessive consumption in one organelle affect other NAD pools? This question becomes particularly relevant in view of the observed decline of tissue NAD^+ content in some diseases such as mitochondrial myopathies [55,56] and, especially, in aging [57-59]. Decreased NAD^+ content is most often interpreted as a result of excessive NAD^+ consumption or decreased NAD^+ biosynthesis. As a cause for the initial change, this is probably true. However, at equilibrium, synthesis and consumption must have equal rates. Therefore, cause and consequence cannot be readily identified when the change has become stably manifested. In line with this notion, Liu *et al.* have recently established NAD^+ turnover rates in cells and tissues by means of stable isotope labeling and LC-MS based quantification [60]. They demonstrated that NAD^+ levels *per se* are unsuitable to evaluate the activities of cellular NAD^+ synthesis and consumption [60].

So far, the consequences of NAD depletion on physiological functions have been largely studied through pharmacological blockage of NAMPT, for example, using the inhibitor FK866 [45,61-64]. This approach has provided important insights into the acute consequences of the essentially irreversible inhibition of NAD^+ biosynthesis. Increased levels of protein acetylation were observed owing to the ensuing inactivation of sirtuins [65,66]. However, the relevance of these observations to chronically decreased NAD^+ levels, as observed in aging, is unclear.

Here, we present a tunable model system for chronic, compartment-specific NAD^+ depletion in human cells. Expression of the catalytic domain of PARP1 resulted invariably in a ~40% lowered total cellular NAD content, irrespective of the subcellular compartment targeted. NAD^+ depletion was surprisingly well compensated as long as the mitochondrial pool was not directly targeted, consistent with a role of this pool as a cellular NAD buffer. The excessive NAD^+-degrading activity was kinetically counterbalanced by the observed NAD decrease to maintain total NAD turnover constant, a mechanism that could plausibly explain aging-related NAD decline. Our study thus revealed distinct cellular responses to chronically lowered NAD levels that are rather different from acute NAD depletion.

Results

PARP1cd expression decreases cellular NAD^+ content by ~40%, irrespective of the subcellular compartment targeted

We have previously demonstrated that HEK293 (293) cells stably expressing the catalytic domain of PARP1 (PARP1cd) in the mitochondria (293mitoPARP1cd or mP cells) or the cytosol (293cytoPARP1cd or cP cells) represent powerful systems to study these subcellular NAD^+ pools [52,67,68]. To comprehensively analyze the consequences of compartment-specific chronic NAD^+ depletion, we generated two additional cell lines, stably overexpressing PARP1cd in peroxisomes (pexPARP1cd or pP) and the ER (ER-PARP1cd or erP), respectively. PARP1cd,

endowed with an N-terminal EGFP-tag, was targeted to these organelles by adding a C-terminal SKL peroxisomal targeting signal or the ER-targeting sequence of BiP and the KDEL ER retention signal for the ER (Fig. 1A). The resulting proteins consume NAD^+ as a substrate for PAR formation in the targeted compartment of interest [52,53] (Fig. 1B). Immunodetection of PAR in the pP cells (Figs. 1C and 1D), and peroxisomal localization were confirmed by colocalization with the peroxisomal marker PMP70 (Fig. 1D). Surprisingly, unlike in cells transiently expressing ER-PARP1cd (Dölle et al., 2010; VanLinden et al., 2017), PAR formation was undetectable in the stably expressing erP cells (Fig. 1E). Addition of nicotinic acid (NA) to the cell culture did not lead to detectable polymers. However, concomitant overexpression of NA phosphoriboslyltransferase (NAPRT) led to readily detectable PAR accumulation (Fig. 1E). Presumably, PAR degrading activity in the ER is high and the activation of the Preiss-Handler pathway through NAPRT expression led to sufficient NAD^+ supply to maintain a detectable PAR level in this compartment. The correct targeting of the erP construct was confirmed by colocalization with the ER marker calnexin (Fig. 1F).

To exploit PARP1cd as a compartment-specific NAD^+ consumer requires a PAR-degrading activity, that is, a dynamic equilibrium of polymer synthesis and degradation. Otherwise, PARP1cd would be mostly in its maximally PARylated form and inactive. The presence of PAR-degrading activities has been previously verified for mP and cP cells [48,67] and here for erP cells (see above, Fig. 1E). To determine whether PAR degrading activity is present within peroxisomes, pP cells were incubated in presence of the PARP inhibitor 3-aminobenzamide (3AB) and the effect on PAR levels was monitored over time. Since mitochondrial PAR turnover has been previously described for mP cells [67], these cells were used as a positive control. In presence of 3AB, the signal for PAR in pP cells weakened in a time-dependent manner, albeit at a somewhat slower rate than that observed in the mP cells (Fig. 1G). Pre-incubation of the

cells in presence of 3AB for 48 hours followed by release of the inhibition showed that polymer levels were readily restored in the pP cells at 24 hours (Fig. 1H). Thus, in pP cells, polymers were restored faster than in mP cells (Fig. 1H). Collectively, these results indicate the presence of PAR-degrading activities and dynamic turnover in all selected organelles. Notably, this is the first demonstration of PAR metabolism in the ER and peroxisomes.

Homogenous expression of the PARP constructs for each cell line used in this study was confirmed by flow cytometry based on the EGFP signal harbored by the recombinant proteins (Fig. S1). However, the level of PARP1cd expression varied somewhat depending on the targeted compartment (Fig. 1I).

Strikingly, the total cellular NAD^+ levels were lowered by approximately 40 % regardless of the compartment targeted (Fig. 1J). Importantly, incubation of the PARP1cd cell lines with 3AB restored cellular NAD^+ concentrations, indicating that the observed NAD^+ depletion was exclusively due to the catalytic activity of the overexpressed constructs (Fig. 1J). Therefore, the established cell lines represent a suitable model system to study chronic, compartment-specific NAD^+ depletion.

Chronic NAD^+ depletion is tolerated surprisingly well by human cells

To assess functional alterations in the PARP1cd cell lines, we first conducted a quantitative proteomics analysis using TMT labeling to establish individual and common changes compared to the parental 293 cell line. Three independent experiments were conducted as replicates for each cell line. Principal component analysis of the protein abundances showed good separation between the different cell lines and clustering of the replicates (Fig. S2A). As shown in Fig. 2A, cP and mP cells exhibited by far the largest amount of proteins whose abundance changed. This might be expected, given that the majority of known NAD^+-dependent

processes take place in the cytosol (and nucleus) and the mitochondria. Interestingly, 112 affected proteins were common for cP and mP, but the direction of change (increase or decrease of abundance) did not always coincide (https://github.com/MolecularBioinformatics/NADpools). Network enrichment analyses (Fig. S2 B-F) showed that among the observed changes across all cell lines, alterations related to protein folding and metabolic processes, especially central carbon metabolism, were most abundant. Some of the effects align with organelle-specific functions for the targeted compartment. For example, carbon metabolism was most affected in mP and cP cells, while protein processing in the ER and peroxisomal processes were among the most abundantly changed in erP and pP cells, respectively. Nevertheless, the changes we observed overall were rather small (https://github.com/MolecularBioinformatics/NADpools) and therefore indicate that chronic NAD^+ depletion evokes relatively mild changes in protein profiles.

We next sought to investigate functional consequences of the subcellular PARP1cd expression. First, we analyzed how NAD^+-dependent processes were affected by NAD^+ depletion in the PARP1cd cell lines. We measured cell proliferation rates and observed no noticeable differences in the PARP1cd cell lines compared to the parental 293 cells (Fig. 2B, solid lines). Blocking NAD^+ biosynthesis by FK866, a NamPT inhibitor, leads to rapid cellular NAD^+ depletion and eventually cell death [48,61,69]. However, in the time frame of the experiment (48h), some loss of cells was observed for cP cells only, while the cell number of the other cell lines remained fairly unchanged indicating growth arrest (Fig. 2B, dashed lines). 3AB caused a partial rescue (Fig. 2B, dotted lines), as it inhibits endogenous and overexpressed PARP activities and thereby reduces NAD^+ consumption and, consequently, the need for its biosynthesis.

Owing to the NAD^+ dependency of sirtuins, changes in cellular NAD^+ levels may severely affect the acetylation state of a variety of proteins [70-72]. Therefore, we compared the protein acetylation state following acute NAD^+ depletion evoked by FK866 treatment in parental cells to that during chronic NAD^+ deficiency in the PARP1cd cell lines (Fig. 2C-E). Acute FK866-mediated NAD^+ depletion in the 293 cells promoted prominent changes. In particular, a strong increase in the acetylation of α-tubulin (Fig. 2C), which is deacetylated by SIRT2 [65,73], as well a decrease in the acetylation of H3K9, likely caused by cell cycle arrest in response to energy depletion [74,75]. In contrast, no major changes were detectable when comparing protein acetylation in whole cell lysates of parental and PARP1cd cell lines (Fig. 2D). The same held true for the acetylation state of proteins in isolated mitochondria (Fig. 2E). These data suggest that the chronically NAD^+-depleted cells have adapted to maintain NAD^+-dependent deacetylation activities even when the concentration of the dinucleotide is substantially decreased.

Direct mitochondrial NAD^+ depletion affects bioenergetics

To assess the potential impact of compartment-specific NAD^+ depletion on energy metabolism, we monitored mitochondrial respiration and glycolysis by measuring the oxygen consumption rate (OCR) and the extracellular acidification rate (ECAR), respectively (Figs. 3A and S3). mP cells displayed considerably lower basal and maximum (uncoupled) respiration rates, as noted previously [68], whereas cP and erP cells exhibited only a slightly reduced maximum respiration (Fig. 3A). Conversely, glycolysis was strongly elevated in mP cells, whereas cP and erP cells were far less affected (Fig. 3A). None of the modified cell lines presented increased leak respiration, supporting that the mitochondrial inner membrane integrity and respiratory control remained intact (Fig S3). PARP1cd expression in peroxisomes

(pP cells) affected neither respiration nor glycolysis. Consequently, the major bioenergetic functions appear to be well maintained during constitutive NAD^+ deficiency, unless the depletion originates from the mitochondria, as is the case in mP cells.

These observations prompted us to employ the resazurin assay, which is an indicator of the activity of mitochondrial NAD^+-dependent dehydrogenases [76] and often used to assess cell viability. Mitochondrial dehydrogenase activities appeared to be maintained in all cell lines regardless of the origin of NAD^+ depletion. Similar to the proliferation measurement in Fig. 2B, the PARP1cd cells were then challenged with FK866. Both mP and pP cells were highly sensitive to this condition displaying a marked decrease already after 24 hours with a further decline after 48 hours whereas cP and erP cells tolerated the treatment for the first 24 hours (Fig. 3B). Regarding pP cells, this finding was surprising, as these cells exhibited normal oxygen consumption rates. Therefore, we assessed the functionality of β-oxidation in the PARP1cd cell lines, an NAD^+-dependent process taking place both in peroxisomes (preferential catabolism of long and very long-chain fatty acids) and mitochondria (preferential oxidation of short/medium chain fatty acids) [77]. As shown in Fig. 3C, under conditions of mitochondrial NAD^+ depletion in mP cells, a dramatic accumulation of medium-chain fatty acids was observed, whereas peroxisomal NAD^+ depletion (pP cells) resulted only in a slight increase of very long-chain fatty acids. Since the NAD^+ dependency of peroxisomal and mitochondrial fatty acid oxidation is similar, it appears that peroxisomal NAD^+ depletion is well compensated, whereas mitochondrial NAD^+ depletion results in a comparatively severe deficiency of β-oxidation.

Taken together, PARP1cd cells cope surprisingly well with the constitutive, targeted depletion of NAD^+. These observations indicate that, unlike during acute NAD^+ depletion, cells can adapt to chronic NAD^+ deficiency and efficiently maintain physiological functions under these

conditions. However, the pronounced functional deficiencies in mP cells demonstrate that targeted depletion of the mitochondrial NAD^+ pool may have severe consequences on cellular homeostasis.

Total cellular NAD^+ turnover is not increased by PARP1cd overexpression

Next, we wished to understand the mechanism how the PARP1cd cells maintained their phenotypic homeostasis despite the lowered NAD^+ concentrations. These are stable cell lines that have attained a steady state. Therefore, to achieve this equilibrium, an augmented NAD^+ consumption could be counterbalanced by an equal increase in biosynthesis. To test this possibility, we determined the NAD^+ turnover using stable isotope labeling-based flux measurements. We substituted the respective unlabeled cell culture medium components by ^{15}N Nam (32μM) and ^{13}C glucose (25mM) and measured the time course of label incorporation into NAD^+ and concomitant decrease of unlabeled dinucleotide using LC-MS. This approach enables the labeling of NAD^+ in both the Nam moiety and the two riboses (Fig. 4A). Therefore, eight different isotopologs can be synthesized (Fig. 4B): NAD^+, NAD^+ M+1 (only labeled in the Nam moiety), NAD^+ M+5 (labeled in one of the two riboses), NAD^+ M+6 (labeled both in Nam and one of the two riboses), NAD^+ M+10 (labeled in both riboses) and NAD^+ M+11 (labeled in Nam and both riboses). Time-course analyses of NAD^+ labeling in 293 cells incubated with the labeled precursors are shown in Fig. 4B. The predominant isotopologs are M+6 and M+11. Fragmentation of NAD^+ M+6 by MS-MS analysis revealed that the labeled ribose originates from the incorporation of PRPP into NMN, whereas the incorporation of the ribose originating from ATP (M+10 and M+11) is considerably delayed (Figs. 4B and S4A). This observation indicates that NMN is readily formed from Nam and PRPP (resulting in NAD^+ M+6), and that

label incorporation from PRPP into ATP proceeds more slowly, presumably because the cellular ATP concentration is high and therefore takes more time to become isotope-labeled. We then applied this approach to the PARP1cd cell lines. As can be inferred from Figures 4C and S4B, the NAD^+ half-lives were considerably shorter than that measured for the 293 control cells. Strikingly, mP and pP cells showed the strongest and nearly identical decrease in their half-lives (2h13 $\pm$ 3 min and 2h17 $\pm$ 3 min). NAD^+ half-lives were also shorter for cP and erP, although to a smaller extent, indicating that, depending on subcellular localization, NAD^+ depletion may affect cellular NAD^+ turnover differently. However, to appropriately compare the NAD^+ turnover (the number of NAD^+ molecules synthesized and consumed per unit of time per cell), we had to take into account the actual NAD^+ contents in the different cell lines (Fig. 1J). As shown in Figure 4D, the observed decrease in NAD^+ half-life in the PARP1cd cell lines can be primarily ascribed to their lower NAD^+ content. Remarkably, NAD^+ turnover did not increase in any of the engineered PARP1cd cell lines, despite the constitutive overexpression of an additional NAD^+ consumer. The mP and pP cells exhibited NAD^+ turnover similar to that of the control cells. That is, their NAD^+ biosynthesis and consumption are essentially the same as those measured for the parental cell lines. On the other hand, cP and erP cells displayed an even slower NAD^+ turnover (Fig. 4D). Intuitively, this may seem paradoxical, since PARP1cd overexpression should increase cellular NAD^+ consumption and, in turn, biosynthetic rates to maintain the steady state. To explain this phenomenon, we used a kinetic model of NAD^+ metabolism (https://github.com/MolecularBioinformatics/NADpools) to simulate PARP1cd overexpression. As shown in Figure 4E, the model recapitulates the observations of the experiments (Fig. 4D) when arbitrarily assuming different maximal NAD^+ consuming activities (10 and 20% increase). However, in the steady state, these maximal activities are not attained, because of a kinetic counterbalancing due to the lowered NAD^+ concentration. That is, the Km

values of the NAD^+ consumers (both endogenous and PARP1cd) are in the range of the (free) NAD^+ concentrations in the cell [41,78]. Therefore, a decrease of the NAD^+ concentration will cause a decrease of the overall NAD^+ consumption rate until the biosynthetic rate is matched (Fig. 4F). These observations indicate that cells might maintain a rather stable NAD^+ biosynthesis rate. In turn, when the total capacity (Vmax) of NAD^+ consumers rises (for example, increased expression of NAD^+-dependent signaling enzymes), unchanged NAD^+ synthesis would limit total cellular NAD^+ consumption kinetically.

Stable NAD^+ biosynthesis kinetically limits NAD^+ consumption

To consolidate this surprising finding, we analyzed the expression of enzymes involved in NAD^+ biosynthesis. Under the conditions of our experiments, the only precursor added was nicotinamide, NAD^+ biosynthesis proceeded via NamPT and NMNAT, the only intermediate being NMN (Fig. 5A, right). The contribution of *de novo* NAD^+ synthesis from tryptophan in our cell lines was likely negligible because inhibition of NamPT by FK866 led to rapid growth arrest and eventually cell death (Figs. 2B and 3B). As shown in Figure 5B, the expression of NamPT was similar in all PARP1cd overexpressing cell lines and seemed unchanged compared to the parental 293 cell line. The proteomics analyses confirmed this evaluation and revealed a decrease only in cP cells (~25%, Fig. S2G). Mathematical modelling of NAD^+ metabolism indicates that even a small change in NamPT activity could have noticeable consequences on NAD^+ turnover (Fig. 5C). Next, we analyzed the presence of the individual NMNAT isoforms in the different cell lines. We did not consistently detect peptides from these enzymes in the proteomics analyses, presumably because tryptic digestion of these proteins generates many small and few rather large peptides. Therefore, we used Western blotting to reveal potential changes in NMNAT abundances. The most noticeable and only significant adjustment in the

expression of NMNATs was observed in mP cells where NMNAT2 was upregulated by approximately 3-fold, suggesting an increased NAD^+ forming capacity in the cytosol (Figs. 5D, E, F).

We wondered whether there may have been constraints on the activity/expression of NamPT that precluded an upregulation of NAD^+ biosynthesis. To test this, we included an alternative precursor, nicotinic acid (NA). This precursor enters NAD^+ biosynthesis through the Preiss-Handler pathway [31,79], which is independent of NamPT (Fig. 5A). It was previously established that NA can sustain NAD^+ synthesis and cell growth in 293 and mP, when NamPT is inhibited by FK866 [48]. Under this condition, the NAD pool is replenished using NA (Fig. S5) indicating that this pathway is functional and active in the cell lines used in the present study. To measure the contribution of NA consumption to overall NAD^+ biosynthesis in our cell lines, we made use of ^{13}C-labeled NA [80]. We did not observe any increase in the use of NA as NAD^+ precursor in the cells expressing PARP1cd compared to the parental cells (Fig. 5G) confirming that upregulation of NAD^+ biosynthesis was generally not used as a compensatory mechanism to counteract increased NAD^+ consumption. Surprisingly, utilization of NA was even significantly diminished in mP cells (Fig. 5G). Indeed, the proteomics analyses revealed a decrease in abundance of NAPRT in these cell lines by about 50% (Fig. S2G). On the other hand, overexpression of NAPRT can increase NAD^+ synthesis from NA, because it enabled the accumulation of PAR in the erP cells (Fig. 1E).

Collectively, these results indicated that, independent of the compartment harboring the overexpressed NAD^+ consumer, NAD^+ biosynthesis was not increased to counterbalance the increased NAD^+ consumption. Rather, by maintaining the expression level of NamPT, the rate-limiting enzyme [81], unchanged NAD^+ consumption was kinetically limited, which is consistent with the observations from the turnover experiments (Fig. 4).

Direct, but not indirect depletion of mitochondrial NAD^+ is detrimental to cellular homeostasis

As opposed to the cells expressing PARP1cd in the cytosol, peroxisomes or ER, mP cells exhibited noticeable phenotypic changes that indicated adverse effects including deficiencies in energy metabolism, fatty acid oxidation and increased NMNAT2 expression. Consequently, the mitochondrial NAD^+ pool appears to play a particular role for cellular NAD^+ homeostasis. To assess the mitochondrial contribution to NAD^+ metabolism of the entire cell, we compared the time courses of labeled Nam incorporation into mitochondrial and whole-cell NAD^+ in 293 cells. Cells were grown on 10 cm dishes, harvested at the times indicated and mitochondria isolated, while a sample was taken to determine label incorporation into total cellular NAD^+. As shown in Figure 6A, left panel, label incorporation into the mitochondrial NAD^+ pool closely followed that of total cellular NAD^+, albeit with a small but reproducible delay. When the same experiment was carried out with mP cells, the relative delay of mitochondrial NAD^+ labeling became appreciably larger (Fig. 6A, middle panel). For comparison, we also analyzed the pP cells (Fig. 6A, right panel), because they exhibited a similar total cellular NAD^+ turnover (Fig. 4D). The relative delay between total and mitochondrial NAD^+ synthesis was similar to that in the control 293 cells (Fig. 6A). To enable calculation of mitochondrial NAD^+ turnover, we estimated the mitochondrial NAD^+ concentration in 293, mP and pP cells. The NAD^+ content in mitochondria isolated from mP cells was dramatically lowered by approximately 80% (Fig. 6B). Strikingly, a strong NAD^+ decrease was also found for mitochondria isolated from pP cells. To validate these measurements, we made use of HeLa cells constitutively expressing a genetically encoded NAD^+ biosensor in mitochondria [41]. Transient expression of the mitochondrial or peroxisomal PARP1cd constructs in these cells demonstrated a similar decline of the free mitochondrial NAD^+ concentration as observed in the corresponding 293-derived PARP1cd cell lines (Fig. 6C). Inhibition of PARP activity by 3AB restored original NAD^+

levels in mitochondria. Treatment of the sensor-cells alone with FK866 strongly diminished free mitochondrial NAD^+ concentration, as expected. Based on these measurements, we calculated the mitochondrial and extramitochondrial (that is, total minus mitochondrial) NAD^+ turnover in these cell lines (Fig. 6D). While the total turnover in 293, mP and pP cells was similar (Fig. 4D), the subcellular distribution of NAD^+ turnover turned out to be very different. In the parental cells, mitochondrial NAD^+ turnover is almost as fast as the extramitochondrial one, while in mP cells, mitochondrial NAD^+ turnover is ten times slower compared to the extramitochondrial one. That is, even though mP cells express an additional NAD^+ consumer (PARP1cd) in the mitochondria, NAD^+ turnover is drastically slowed. Even more striking, mitochondria from pP cells showed a similar behavior (Fig. 6D). These observations suggest that mP cells have adapted to the presence of the PARP1cd construct in mitochondria by dramatically decreasing the mitochondrial NAD^+ content, thereby kinetically minimizing the activity of the construct. On the other hand, in pP cells we also observed a mitochondrial NAD^+ depletion. This would indicate that mitochondria might compensate for the elevated NAD^+ consumption in peroxisomes by providing NAD^+. Indeed, despite a similar total decrease of NAD^+ in the pP and mP cells, targeting the PARP1cd construct to peroxisomes resulted in only subtle functional deficiencies.

NMNAT3 is not required for mitochondrial NAD^+ generation

A putative buffering function of the mitochondrial NAD^+ pool would be intrinsically linked to the mechanisms underlying the establishment and maintenance of that pool. Recent studies have shown that the main route for the maintenance of mitochondrial NAD^+ levels is associated with SLC25A51/MCART1, an NAD^+ carrier in the mitochondrial inner membrane [49,50]. Therefore, the role of the previously identified mitochondrial NMNAT3 [38,82] in

mitochondrial NAD^+ homeostasis is unclear. Moreover, it was recently shown that NMNAT3 is not vital in mice [51]. To verify whether NMNAT3-deficient mitochondria from human cells contain sufficient NAD^+, we used CRISPR/Cas9-edited HAP1- *Nmnat3* $^{-/-}$ cells. As shown in Figure 7A, the NMNAT3 protein was indeed undetectable in the KO cell line. Importantly, when analyzing mitochondrial PAR generation following overexpression of mitochondrial PARP1cd, WT and KO cells were essentially indistinguishable, indicating similar mitochondrial NAD^+ contents (Figs. 7B and C). The undiminished content of NAD^+ in the mitochondria from the *Nmnat3*$^{-/-}$ cells is unlikely a result of a redistribution from other subcellular pools, because the total cellular NAD^+ in WT and KO cells is also similar (Fig. 7D). These results are consistent with the notion that, even in a cell normally expressing NMNAT3, this enzyme is not required to maintain mitochondrial NAD^+ levels. Consequently, the enzyme may not be solely involved in mitochondrial NAD^+ biosynthesis. In fact, the NMNAT-catalyzed reaction is fully reversible [38,83], the equilibrium favoring the production of NMN and ATP from NAD^+ and pyrophosphate (PPi) (Fig. 7E). Therefore, in cooperation with SLC25A51/MCART1, NMNAT3 could act as a rheostat buffering cellular NAD^+ levels according to demand (Fig. 7E).

Discussion

The present study has provided fundamentally new insights into the physiology of intracellular NAD^+ pools, their interconnectivity, dynamics and plasticity. To explore NAD^+ biology on a subcellular level, we established and analyzed human cell lines stably expressing an NAD^+ consumer targeted to various subcellular compartments. The use of the catalytic domain of PARP1 as targeted NAD^+ consumer has several advantages. The protein can be easily targeted (as it lacks the nuclear localization signal of full-length PARP1). Moreover, it retains its catalytic activity when fused to GFP, a feature that makes it easy to monitor proper subcellular

localization and homogenous expression within a cell population. The possibility to immunodetect PAR as an indicator of the catalytic activity is a further advantage, even though PAR is not detectable in cP and erP cell lines, despite the activity of the construct [52]. Perhaps, the most important advantage is the availability of specific PARP inhibitors permitting to control the catalytic activity, that is, making it a tunable system that does not rely on drug-inducible expression.

Chronic cellular NAD^+ deficiency reveals unexpected adaptive mechanisms

In addition to the organelle-specific NAD^+ depletion, our model system enabled the experimental study of chronic rather than acute NAD^+ deficiency in human cells. Many investigations have made use of potent NamPT inhibitors such as FK866 to identify the consequences of acute NAD^+ depletion [45,61-64]. Treatment of cells with FK866 causes rapid NAD^+ loss in 293 cells, commensurate with the NAD^+ turnover rate determined in the present study. Under these conditions, the equilibrium between synthesis and degradation is disrupted, as NAD^+ synthesis is essentially switched off, while degrading enzymes continue cleaving the remaining NAD^+, albeit with decreasing activity owing to the declining NAD^+ concentration. The diminished activity can be noted, for example, by increased levels of protein acetylation owing to decreasing sirtuin-dependent deacylation. In the end, the cells die because of insufficient NAD^+ supply [84,85]. Given the inevitable outcome, it is not obvious whether the observed effects of acute NAD^+ depletion reflect adaptive mechanisms or unregulated consequences of cell death.

In contrast, chronic NAD^+ shortage, as evoked in our cell lines, requires the establishment of a new equilibrium between NAD^+ synthesis and consumption. In principle, when the total number of NAD^+ consumers (Vmax) increases, this could be counteracted by increasing the

activity of NAD^+ biosynthesis to match the higher demand. Such a response would result in an increased cellular NAD^+ turnover (Fig. 4E and F). Surprisingly, our measurements revealed that the common response to PARP1cd overexpression was no change or even a slight decrease in NAD^+ biosynthesis (erP and cP cells) and, hence, NAD^+ turnover. Mathematical modelling showed that the robust maintenance of the NAD^+ biosynthesis flux (as primarily reflected by unchanged expression of NamPT, the rate-limiting enzyme) is an appropriate adaptive mechanism, because, in the steady state, consumption can only be as fast as biosynthesis (Fig. 4). However, as a consequence, the total cellular NAD^+ level needs to decrease. Thereby, NAD^+-consuming enzymes are kinetically downregulated, due to diminished substrate saturation, until the consumption rate again matches that of NAD^+ synthesis. Thus, a new steady state is attained with the same total turnover as originally present in the parental cells. Accordingly, NAD^+-dependent functions are relatively well maintained, despite a considerably lowered NAD^+ concentration (Fig. 2 and 3).

Strikingly, the fact that the changes observed in the PARP1cd cell lines can be well described by a purely kinetic model of NAD^+ metabolism (Fig. 4F) indicates that there are no discernable signaling mechanisms governing NAD^+ homeostasis. We conclude, therefore, that the general cellular maintenance of NAD^+ homeostasis is regulated primarily based on enzyme kinetics. Consistent with this notion, according to the KEGG database [86], as many as ~25% of all biochemical reactions use NAD(P) as cofactor, a number that would make it inconceivable to invoke regulation of specific enzymes to regulate global NAD^+ homeostasis. The only noticeable adaptation of NAD^+ synthesis was the increased expression of NMNAT2 in mP cells. Interestingly, NMNAT2 has been shown to be upregulated during adipocyte differentiation to support cytosolic NAD^+ synthesis [42]. Therefore, this enzyme seems to emerge as a key player in controlling the distribution of NAD^+ into different subcellular pools.

Subcellular NAD^+ pools interact to maintain global NAD^+ homeostasis

A surprising finding was that, regardless of its subcellular location, the constitutive activity of PARP1cd led to a decrease of the total cellular NAD^+ content to about 60% of the parental cell line. A plausible interpretation of this observation is that the remaining amount of NAD^+ represents a minimum to maintain viability. Cells that might acutely tolerate even lower NAD^+ contents cannot survive the long-term depletion during the generation and maintenance of stably transfected PARP1cd cell lines. On the other hand, the convergence to the same remaining NAD^+ content in all the PARP1cd cell lines points towards a hitherto undetected dynamic interplay between the different subcellular NAD^+ pools and suggests the presence of mechanisms that sense and redistribute the total cellular NAD^+ content upon local depletion. Indeed, the concentration of NAD^+ in mitochondria is known to be substantially higher than in other subcellular compartments [41,78], and the NAD^+ metabolism of these organelles has been proposed to be autonomous [45,46]. Nevertheless, even in mitoPARP1cd cells, the same total cellular NAD^+ concentration was attained. Thus, our data provide evidence that a redistribution of cellular NAD^+ pools takes place to match the essential demands in all compartments. Of note, however, despite being the pool with the highest NAD^+ concentration under normal conditions [41,78], direct constitutive depletion of mitochondrial NAD^+ causes severe functional deficiencies. Consequently, mitochondria can provide NAD^+ to maintain other pools, but are insufficiently supported when in critical demand themselves.

Mitochondrial NAD^+ homeostasis is critical to maintain cellular functions

We found that the incorporation of precursors into mitochondrial NAD^+ is slightly delayed relative to the other pools (Fig. 5). This observation indicates that the uptake of NAD^+ into

mitochondria is rate-limiting for the maintenance of mitochondrial NAD^+. When mitochondrial NAD^+ is subjected to degradation by the expression of mitoPARP1cd, the mitochondrial NAD^+ turnover is strongly reduced, and the delay becomes more pronounced (Fig. 5). This may seem paradoxical, since overexpression of an NAD^+ consumer should increase the turnover. However, it turned out that the mitochondrial NAD^+ content in the mP cells is dramatically diminished. Presumably, to minimize NAD^+ cleavage by the overexpressed construct, the concentration of mitochondrial NAD^+ was strongly decreased. Thereby, even the activities of other NAD^+-dependent processes were affected resulting in the overall decrease of mitochondrial NAD^+ turnover. Importantly, when assessing mitochondrial NAD^+ content and turnover in pP cells, these were also strongly decreased. Notably, mP cells exhibited a strong accumulation of short- and medium chain fatty acid esters (Fig. 3C) and a substantially lower rate of oxidative phosphorylation (Fig. 3A), both NAD^+-dependent mitochondrial processes. In contrast, despite the considerable mitochondrial NAD^+ depletion, pP cells did not exhibit any measurable OXPHOS deficiency, while the resazurin assay revealed only a slight increase of sensitivity of mitochondrial NAD^+-dependent dehydrogenases when challenged with FK866 (Fig. 3B). Moreover, the abundance of long-chain fatty acids appeared to be only slightly elevated indicating that a major NAD^+-dependent peroxisomal process was only marginally affected despite cellular NAD^+ depletion originating from these organelles. Likewise, we did not detect any noticeable defects in bioenergetic or other NAD^+-dependent functions in cP or erP cells. Since the overall NAD^+ decrease was similar in all engineered cell lines, mitoPARP1cd cells clearly stand out with their vulnerability when these organelles represent the origin of enhanced NAD^+ degrading activity. As exemplified by the pP cells, mitochondria appear to have the capacity to support NAD^+-dependent functions in other subcellular compartments.

Mitochondrial NAD^+ metabolism is compatible with a function as cellular NAD^+ rheostat

Mitochondria are known to have the highest subcellular NAD^+ concentration in a variety of cell lines, including in 293 cells [41,78]. So far, the reason for this NAD^+ accumulation in mitochondria has remained unclear. Considering the results from the present study, we propose that mitochondria may serve as an NAD^+ reservoir to buffer fluctuations in cellular NAD^+ concentrations. This suggestion is consistent with previous studies demonstrating the important role of the mitochondrial NAD^+ pool for cell vitality and the detrimental effects when this pool is impaired [45,46,68].

It has recently been reported that SLC25A51 is a mitochondrial NAD^+ carrier essential to maintain the mitochondrial NAD^+ pool in mammals [49,50]. The majority of the SLC25 family of mitochondrial carriers are known to be reversible exchange carriers [87,88]. Therefore, in principle, SLC25A51 might also mediate the export of NAD^+ from mitochondria, on demand (Fig. 7E). On the other hand, NMNAT3 has been proposed to catalyze the generation of NAD^+ from NMN and ATP in mitochondria, which would require NMN uptake into the organelles [48]. However, it has been shown that *Nmnat3*$^{-/-}$ mice are viable [51]. Indeed, as we demonstrate here, knocking out NMNAT3 in HAP1 cells (which normally express NMNAT3 and SLC25A51) did not affect mitochondrial or whole cell NAD^+ content (Fig. 7B-D). Given the reversibility of both the mitochondrial NAD^+ carrier and the reaction catalyzed by NMNATs, it appears plausible that mitochondria may fulfill their function as cellular NAD^+ buffer by maintaining an appropriate balance based on the cooperation between SLC25A51 and NMNAT3. In such a scenario, depending on the extramitochondrial NAD^+ demand, mitochondrial NMNAT3 would generate NAD^+ for export when needed or, when demand outside the organelles is low, imported NAD^+ is cleaved to NMN and ATP, thereby maintaining a readily available reserve for rapid NAD^+ production.

Methods

Cell culture

293 cells were cultivated in Dulbecco´s modified Eagle's medium supplemented with 10% (v/v) fetal calf serum (FCS), 2 mM glutamine, and penicillin-streptomycin. HeLaS3 cells were grown in Ham's F12 medium supplemented with 10% (v/v) FCS, and penicillin-streptomycin. HAP1 cells were cultured in Iscove's Modified Dulbecco's Medium supplemented with 10% (v/v) FCS, 2 mM L-Glutamine, and penicillin-streptomycin. The cells were cultured at 37 °C in a humidified atmosphere of 5% CO_2 (standard culture conditions).

293 and HeLaS3 cells were obtained from the American Type Culture Collection (ATCC, Manssas, VA). Wild type and NMNAT3 knock-out HAP1 cells were obtained from Horizon.

For the generation of stably transfected cell lines, 293 cells were transfected by the calcium phosphate precipitation method. Cell lines were generated after two rounds of selection in presence of 550 µg/ml G418 and were maintained in complete 293 medium supplemented with 550 µg/ml G418.

Cell proliferation and viability

Cell proliferation and viability were determined by flow cytometry. For proliferation, 50,000 cells/well were seeded in the cavities of a 12-well plate. Cells were washed with PBS and trypsinized with 200 µl trypsin/EDTA for 5 min at 37 °C. Trypsinized cells were centrifuged (350 x g, 5 min) and resuspended in 1 ml ice-cold PBS prior to analysis. For assessment of FK866 sensitivity, 50,000 cells were seeded in triplicate in the cavities of a 12-well plate prior to treatment with FK866 (2 µM) with or without 3-aminobenzamide (3AB, 1 mM)). After incubation for the indicated time points, samples were prepared as described above. Cell

counting was performed on a BD Accuri C6 flow cytometer according to the manufacturer's guidelines. Data analysis was conducted using FlowJo X. Cells were gated to exclude debris, followed by standard doublet exclusion.

Resazurin-based in vitro toxicology assay

To assess mitochondrial NAD-dependent dehydrogenase activity, a resazurin-based in vitro toxicology assay kit was used (Sigma). For assessment of FK866 sensitivity, 10,000 cells per well were seeded in the cavities of 96-well plates and the cells were treated with either Dimethylformamide (solvent for FK866), FK866 (2 µM) or FK866 (2 µM) and 3AB (1 mM) for the indicated time points. For analysis, the medium was replaced with fresh complete medium supplemented with 10% (v/v) resazurin, and the cells were incubated for 2 h. Fluorescence was detected using a BMG LabTech FLUOstar Optima plate reader with a 540/10 nm excitation filter and a 590 nm emission filter. Fresh complete medium containing 10% (v/v) resazurin served as a blank.

Protein determination, SDS-PAGE and Western blot analysis

Cells were washed with PBS and lysed in 20 mM Tris/HCl (pH 7.4), 1 mM EDTA, 2% (w/v) SDS, 150 mM NaCl, and 1 mM 3AB. Genomic DNA was sheared by passage through a syringe with a 23 Gauge needle. Protein concentration was determined using BCA reagent (Thermo Fisher Scientific-Pierce). SDS-PAGE and immunoblot analyses were performed according to standard procedures. Enhanced chemiluminescence (SuperSignal Wset Dura, ThermoFisher Scientific) was used for immunodetection. Images were acquired using a ChemiDoc XRS+ and ImageLab software (Bio-Rad).

Immunocytochemistry

Cells were grown on poly-L-lysine-coated coverslips and fixed for 15 min with ice-cold 4% (w/v) paraformaldehyde in PBS. After 15 min permeabilization with 0.5% (v/v) Triton X-100 in PBS and subsequent blocking with complete medium for 1 h, primary antibodies diluted in complete medium were added to cells followed by overnight incubation at 4 °C. After washing with PBS and PBS-T (PBS with 0.1% (v/v) Triton X-100) and subsequent 1 h-incubation with AF594- and AF647-conjugated secondary antibodies in complete medium at RT and further 10 min DAPI-staining, the slides were washed with PBS and PBS-T prior to mounting onto slides. Images were taken using a Leica TCS SP8 STED 3x confocal laser scanning microscope equipped with a ×100 oil immersion objective (numerical aperture 1.4).

Measurement of cellular glycolytic rate and oxygen consumption rate

Oxygen consumption rate (OCR) and extracellular acidification rate (ECAR) in 293 cells were measured by the use of the Seahorse XF^{e}96 Analyzer (Agilent, Santa Clara, CA, US). The experimental procedure was performed essentially as described earlier (VanLinden et al., 2015). The microplates were coated with collagen type I (1 mg/ml in 0.1 M acetic acid) for 2 hh, washed with PBS and air-dried overnight. 30,000 cells/well were seeded in the coated microplates the day before analysis. For analysis of mitochondrial respiratory function, the OCR measured in unbuffered assay medium (pH 7.4, containing 2 mM L-glutamine, 2 mM sodium pyruvate and 10 mM glucose) was determined as basal respiration. Thereafter, successive injections of 3 µM oligomycin (leak activity), 1 µM CCCP (respiratory capacity), 1 µM rotenone (complex I-independent respiration) and 1 µM antimycin A (non-mitochondrial respiration) were conducted to investigate mitochondrial respiratory function. For measuring glycolysis function, the basal ECAR was measured in unbuffered assay medium (pH 7.4,

containing 2 mM L-glutamine). This was followed by an injection of 10 mM glucose to measure glycolysis-dependent ECAR. Next, 3 µM oligomycin (glycolytic capacity) and finally 100 mM 2-deoxyglucose (non-glycolytic ECAR) were added. All data were normalized to protein content, measured using BCA reagent as previously described.

Fatty acids analyses

Fatty acids were quantified as Fatty Acid Methyl Esters (FAMEs) by gas chromatography. Cells were grown to confluency in 15 cm dishes. Following trypsinization, the cells were collected in 8 ml fresh medium and centrifuged at 350 x g for 5 min. The pellet was washed with 5 ml PBS, followed by a second centrifugation after which the pellet was resuspended in 200 µl PBS. The samples were stored at -20 °C under nitrogen atmosphere. Prior to analysis, 100 µl internal standard (C21:0 FAME dissolved in isooctane, c = 0.1956 mg/ml) were added to the samples and fatty acids were derivatized to FAMEs by direct esterification with methanolic HCl as described by Meier, et al. [89]. The extracts were diluted 1:5 with isooctane before analysis by gas chromatography. FAMEs were analyzed on a 7890 gas chromatograph (Agilent) equipped with split-splitless injector, flame ionization detector and a BPX70 capillary column (SGE, Ringwood, Australia) as previously described with minor adjustments to the temperature program [90,91]. Identification and quantification were performed in Chrombox C (www.chrombox.org) based on templates from previous analyses of human serum and plasma by gas chromatography coupled to mass spectrometry [92]. Chromatographic areas were corrected by empirical response factors based on the reference mixture GLC-793 (Nu-Chek Prep. Elysian, MN, USA) that was run as every 6th sample in the analytical sequence.

NAD^+ biosensor calibration

NAD^+ biosensor calibration was conducted essentially as described earlier [41]. 500,000 HeLa cells stably expressing the NAD biosensor in the cytosol or the cpVenus control [41] were washed with 1 ml PBS and trypsinized with 200 µl trypsin/EDTA for 5 min at 37 °C with 5% CO_2. Trypsin was inactivated by the addition of 0.8 ml fresh complete medium and the cells were centrifuged at 300 x g for 5 min. Following centrifugation, the supernatant was discarded and the pellet was resuspended in 1 ml permeabilization buffer (20 µg/ml digitonin; 100 mM KCl; in 1 × PBS) and equilibrated at RT for 15 min with indicated NAD^+ concentrations. Additionally, control cells were permeabilized in the presence of 50 µg/ml propidium iodide (20 µg/ml digitonin, 50 µg/ml PI, 100 µg/ml RNAse A in 1 x PBS) to ensure complete permeabilization. Data collection was conducted on a BD LSRFortessa using 407-F (ex. 407 nm, em. 525/50 nm BP filter) and 488-C (ex. 488 nm, em. 530/30 nm BP filter) for sensor fluorescence intensity, and 561-E (ex. 561 nm, em. 582/15 BP filter) for PI fluorescence intensity. Cells were gated to exclude debris, followed by standard doublet exclusion, and at least 10,000 cells were collected per sample. Data analysis was conducted using the FlowJo X software with debris and doublet exclusion followed by determination of the geometric mean of the fluorescence intensity. Ratiometric 488/405 nm fluorescence values from the sensor were normalized to the fluorescence from the corresponding cpVenus control. Values from 5 independent experiments were fit to a sigmoidal regression model using GraphPad Prism 8 (y=min+[(min−max)1+10($logEC50-x$)×$HillSlope$]) with a 95% confidence interval.

Quantification of mitochondrial free NAD^+ using the biosensor

200,000 HeLa cells that either stably express the NAD biosensor or the cpVenus control [41] in the mitochondria were seeded in the cavities of a 6-well plate. On the next day, the cells were transfected with red PARP1cd constructs (mKate2-PARP1cd-SKL or MTS-mKate2-PARP1cd-

myc) in the absence or presence of 1 mM 3AB using the XtremeGENE 9 transfection reagent according to the manufacturer's instructions (Merck). Alternatively, cells were incubated with 2 µM FK866 or its solvent DMF. After 48 h, the cells were washed with 1 ml PBS and incubated with 200 µl Trypsin/EDTA for 5 min at 37 °C with 5% CO_2. Trypsin was inactivated by addition of 800 µl of freshly prepared medium (HEPES-buffered phenol red-free complete DMEM). The samples were stored on ice and analysed using a BD LSRFortessa with a 407-F (ex. 407 nm, em. 525/50 nm BP filter) and a 488-C (ex. 488 nm, em. 530/30 nm BP filter) for sensor fluorescence intensity, and 561-E (ex. 561 nm, em. 661/20 BP filter) for mKate2 fluorescence intensity. Cells were gated to exclude debris, followed by standard doublet exclusion, and at least 10,000 cells were collected both in the mKate2/PARP1cd positive and the mKate2/PARP1cd negative gates. Data analysis was conducted using the FlowJo X software with debris and doublet exclusion followed by determination of the geometric mean of the fluorescence intensity. Ratiometric 488/405 nm fluorescence values from the sensor were normalized to the fluorescence from the corresponding cpVenus control and interpolated with the calibration curve using GraphPad Prism 8. The change in concentration between positively and negatively transfected cells was then calculated in percent for each sample. Alternatively, the change in concentration upon treatment with 2 µM FK866 was calculated in percent compared to the solvent control.

Synthesis of the ^{15}N Nam

Nicotinamide (8 g, 65.51 mmol) and 1-chloro-2,4-dinitro-benzene (14 g, 69.12 mmol) were melted together at 110oCand mixed for around 1 h until the orange solution hardened. The resulting orange glass like material was dissolved in MeOH and absorbed onto a minimal amount of silica and transferred as dried material to a 340 g biotage column. Once placed, a

gradient of 0% MeOH: 100% EtOAc to 6 (EtOAc) : 4 (MeOH) (v/v) was applied which ran over 2.5 L. Care was taken to prevent the product from crashing out on the column and block solvent flow. The excess chlorodinitrophenyl was isolated first then the unreacted nicotinamide and finally the Zincke salt in 19.83 g quantity as an orange solid. ^{1}H NMR consistent with the literature.

^{15}N ammonium chloride (2.35 g, 42.39 mmol) and TEA (11.53 ml, 82.74 mmol) was added into a 500 ml RBF containing 200 ml of MeOH (non-dry but from a fresh Winchester bottle) at 0 °C using ice bath. After stirring for 20 min a solution of 1-(2,4-dinitrophenyl)pyridine-3-carboxamide (11.83 g, 40.76 mmol) dissolved in 100 ml MeOH (non-dry) was added dropwise at RT over ~60 min at 0 °C. The solution was allowed to warm to RT. The deep red color faded to an orange colour but by TLC (80% EtOAc : 20% MeOH) the starting material had disappeared and the dinitro by-product and nicotinamide was evident. The solution was concentrated and suspended in water. Thorough mixing (to dissolve the nicotinamide) and filtration through cotton wool syringe provided an aqueous layer with just nicotinamide and traces of the dinitro by-product. The aqueous layer was concentrated and purified by silica column chromatography using a 100% EtOAc to 8:2 (EtOAc:MeOH) over 2000 ml on a 340 g silica biotage column. The traces of dinitro by-product eluted first and then ^{15}N nicotinamide, as 3.555 g of an off white solid. ^{1}H NMR was consistent with the literature.

Isotopic labeling, nucleotide extraction and LC-MS analyses

250,000 cells per well were seeded in the cavities of a 12-well plate and incubated at 37 °C with 5% CO_2 overnight. When needed, isotopic labeling using 13C glucose (25 mM) (Cayman Chemical), 15N nicotinamide (33 μM) or 13C nicotinic acid (100 μM) was performed as follows.

On the day before the experiment started, medium was exchanged for medium containing dialyzed serum. On the next day, at T0, medium was exchanged for medium containing the labelled compounds and samples were collected at the indicated time points.

For sample collection, cells were placed on ice, the medium was removed, and the cells were washed twice with 0.5 ml ice-cold PBS. Then 0.5 ml ice-cold 80% (v/v) LC-MS grade methanol was added to each well and the cells were incubated at 4 °C on a shaker for 20 min. After incubation, the cells were detached from the wells using a cell scraper and the samples were transferred to 1.5 ml tubes. To ensure full transfer, the wells were washed twice with 0.3 ml of ice-cold 80% (v/v) LC-MS grade methanol. The samples were subsequently frozen at -80 °C. On the day of liquid chromatography – mass spectrometry (LC-MS) analysis, the samples were thawed on a rotating wheel at 4 °C before centrifugation at 16,000 x g for 20 min at 4 °C. After centrifugation, 0.7 ml of the supernatant was transferred to a new tube and 0.7 ml acetonitrile was added to each sample. Where applicable, samples were further mixed in a ratio of 1:10-1:20 with an internal ^{13}C-labelled standard for the accurate determination of NAD^+ concentration.

Separation of nucleotides by liquid chromatography was achieved on ZIC-cHILC column (100 x 2.1 mm, 3 µm; Merck) in a Dionex UltiMate 3000 coupled to a QExactive mass spectrometer (Thermo Scientific). For analysis, the ZIC-cHILC column was kept at 20 °C. The injection volume for all samples was 10 µl and the flow rate was kept at 0.3 ml/min.

The mobile phase consisted of 20 mM ammonium acetate pH 6.8 (buffer A) and acetonitrile (buffer B). The gradient was set as follows: runs were started with 80 % buffer B for 1 min and reduced to 72 % buffer B over the next 0.2 min. The concentration of buffer B was further decreased to 70 % over 10.8 minutes before being brought to 5 % in the course of 1 min for washout. After 3.5 min at 5 %, the concentration of buffer B was returned to 80% over 1 min

for equilibration. The column was equilibrated at 80 % buffer B for 3.5 min before ending the run. Electrospray ionization was performed using the positive ion polarity mode and a spray voltage of 3.5 kV. Sheath flow gas flow rate was 48 units with an auxiliary gas flow rate of 11 units and a sweep gas flow rate of 2 units. Mass spectra were recorded using targeted single ion monitoring with an isolation window of 17 m/z with automatic gain control set to a target of 5 x 10^5 and maximum accumulation time of 300 ms. Data analysis was conducted in the Thermo Xcalibur Qual Browser (Thermo Scientific).

For normalization to protein content, the pellet was dried overnight and resuspended in 200 µl lysis buffer (20 mM Tris-HCl pH 7.4, 150 mM NaCl, 2% (w/v) SDS, 1% (w/v) EDTA). Protein concentration was subsequently determined using the BCA assay kit (Thermo Scientific) according to the manufacturer's recommendations.

Isolation of mitochondria from cultured human cells

Isolation of mitochondria form cultured human cells was carried out using the MidiMACS® mitochondria isolation kit (Miltenyi Biotech). Confluent cells in a 10 cm dish were washed once with 10 ml PBS and trypsinized with 1 ml trypsin/EDTA for 5 min at 37 °C. Afterwards, the cells were harvested in 9 ml PBS and centrifuged at 300 x g for 10 min at 4 °C. The supernatant was removed, and the pellet resuspended in 10 ml ice-cold PBS. After another centrifugation at 300 x g for 10 min at 4 °C, and the removal of the supernatant, the pellet was resuspended in 1 ml lysis buffer (provided by the kit) containing 1 x protease inhibitor. The cells were carefully lysed by shearing through a 26 gauge needle 20 times. Upon lysis, 9 ml ice-cold 1 x separation buffer were added to the sample, and the crude cell lysates were subsequently incubated with 50 µl anti-TOM22 MicroBeads for 1 h on a rotating wheel at 4 °C. The LS column (Miltenyi Biotech) was placed in the magnetic field of the MidiMACS® Separator (Miltenyi Biotech) and

equilibrated by stepwise addition of 9 ml of separation buffer. After incubation with the labelled beads, the cell lysate was applied onto the column where mitochondria were retained. Following washing with 9 ml of separation buffer, the mitochondria were eluted by addition of 1.5 ml separation buffer and firmly pushing a plunger into the column. The sample was centrifuged at 13,000 x g for 2 min at 4 °C. The supernatant was removed, the pellet resuspended in 1 ml storage buffer and again centrifuged at 13,000 x g for 2 min and at 4 °C. Thereafter, the pellet was either resuspended in 100 µl lysis buffer (20 mM Tris-HCl pH 7.4, 150 mM NaCl, 2% (w/v) SDS, 1% (w/v) EDTA) to allow for western blotting, or in ice-cold 80% (v/v) LC-MS grade methanol to allow for LC-MS analysis and immediately stored at -80 °C. For LC-MS analysis, the samples were thawed on a rotating wheel at 4 °C for 30 min before centrifugation at 16,000 x g for 20 min at 4 °C. After centrifugation, the supernatant was removed and added to 1 volume of acetonitrile prior to analysis. The samples were further mixed in a ratio of 1:5 with an internal C^{13}-labelled standard for the accurate determination of NAD^+ concentration. The samples were subsequently analyzed by LC-MS analysis using the settings described in the section "Isotopic labeling, nucleotide extraction and LC-MS analyses". For normalization to protein content, the pellet was dried overnight and resuspended in 100 µl lysis buffer (20 mM Tris-HCl pH 7.4, 150 mM NaCl, 2% (w/v) SDS, 1% (w/v) EDTA). Protein concentration was subsequently determined using the BCA assay kit (Thermo Scientific) according to the manufacturer's recommendations.

Isotopolog Correction

To correct for natural isotope abundance the python package PICor (https://github.com/MolecularBioinformatics/PICor) was used. It applies a theoretical

isotopolog correction approach based on statistical distributions of each isotopolog. The detailed approach has been described previously [93].

Graphs were plotted with python 3.8 using the python libraries Matplotlib 3.1.3 [94,95] and seaborn 0.10.0 [96].

Determination of cellular half-life and turnover rates

The half-life of NAD was estimated based on fitting an exponentially decay functions (see equation 1) to the measured ratios of unlabeled to total NAD over time (t). The SciPy [97] optimization function curve fitting was used for determining the prefactor A and the exponential factor k along with their respective standard deviations, see equation 2 and 3.

The ratio of unlabeled to total NAD amount ranges between 0 and 1 with no label being present at time point zero. The exponential curve of the unlabeled compound should therefore start at 1 and approaches 0 over time. The prefactor A should therefore be close to 1 and its deviation is an indication for the quality of the fit.

$$(1)\ \frac{NAD_{unlabelled}}{NAD_{total}} = A \cdot e^{-kt}$$

$$(2)\ t_{1/2} = \frac{ln(2A)}{k}$$

$$(3)\ \sigma_{t_{1/2}} = \sqrt{\left(\frac{\sigma_A}{A \cdot k}\right)^2 + \left(ln2A \cdot \frac{\sigma_k}{k^2}\right)^2}$$

Determination of mitochondrial half-life and turnover rates

The cellular NAD pools are connected but have distinct concentrations and turnover rates. As we can only determine whole cell and mitochondrial NAD concentrations and turnover, the parameters for the nucleo-cytoplasm (extramitochondrial) turnover were determined in a

multistep process. First the mitochondrial labeling dynamics were fitted based on the ratio of unlabeled to total NAD in mitochondria, as above:

$$(4)\ \frac{NAD_{unlabelled,mito}}{NAD_{total,mito}} = A_{mito} \cdot e^{-k_{mito}t}$$

To estimate the extramitochondrial turnover, we calculated the distribution of NAD between the nucleo-cytoplasm and mitochondria as follows: The volume of mitochondria and nucleo-cytoplasm were determined in 293 cells using confocal microscopy. Free NAD concentrations in both compartments were measured using the NAD biosensor expressing HeLa cells as described above. These measurements were then used to calculate the mitochondrial and nucleo-cytoplasmic amount of NAD per cell, assuming a ratio of free to bound NAD of 1:10. The amount of mitochondrial NAD in 293 cells stably transfected with PARP1cd was calculated accordingly using the relative differences in mitochondrial NAD measured by LC-MS and the NAD concentrations measured in whole cells.

In a second step, whole cell measurements were used to estimate the turnover rate k_{cyto} of the extramitochondrial fraction of the NAD pool, which is here referred to as "nucleo-cytoplasmic", to simplify descriptions. A sum of two exponential function was used to describe the combined cellular pool using subcellular NAD amounts as scaling factor:

$$(5)\ \frac{NAD_{unlabelled,cell}}{NAD_{total,cell}} \cdot n_{NAD,cell} = A_{cyto} \cdot n_{NAD,cyto} \cdot e^{-k_{cyto}t} + A_{mito} \cdot n_{NAD,mito} \cdot e^{-k_{mito}t}$$

The initial slope s of the dynamics in unlabelled NAD was used to calculate the turnover of NAD. In mathematical terms the NAD turnover is calculated using the first derivative of equation 1 with respect to t at time point $t = 0\mathrm{h}$ multiplied by the total cellular amount of NAD ($n_{NAD_{total}}$) :

$$(6)\ s = \frac{dn_{NAD_u}}{dt}|_{t=0} = A \cdot k \cdot n_{NAD_{total}}$$

$$(7)\ \sigma_s = \sqrt{\left(\frac{\sigma_A}{A}\right)^2 + \left(\frac{\sigma_k}{k}\right)^2 + \left(\frac{\sigma_{n_{NAD}}}{n_{NAD}}\right)^2}$$

The turnover for the nucleo-cytoplasmic and the mitochondria pool were calculated accordingly:

$$(8)\ s_{cyto} = A_{cyto} \cdot k_{cyto} \cdot n_{NAD_{cyto}}$$

$$(9)\ s_{mito} = A_{mito} \cdot k_{mito} \cdot n_{NAD_{mito}}$$

Quantitative proteomics

Cells were cultured as described above. Following trypsinization, 10^6 cells were counted and pelleted by centrifugation for 10 min at 400 x g.

Quantification of proteins and peptides was achieved by an MS/MS-based analysis strategy using isotopomer labels as described previously [98]. Analysis was conducted by the Proteomics Unit at the University of Bergen (PROBE) [99]. To identify significant differences in the proteome of different cell lines, only proteins identified with high confidence (FDR < 1%) were included in the further analysis.

We performed independent parametric t-tests for each protein comparing the abundance ratios of the PARP1cd cell lines versus the 293 cells. Proteins with $p < 0.001$ were interpreted to be significantly differentially expressed. For these significantly changed proteins we calculated mean $\log_2$ fold changes between each PARP1cd cell line and 293 cells.

We then performed Principal Component Analysis (PCA) on the proteins changed with high confidence (FDR > 1%) using scikit-learn 0.23.1 [100]. To ensure equal feature variance, the protein abundances were normalized to their Z-Scores. Components were added until 95% of

total variance was accounted for, which resulted in a total of 21 components. The results were plotted using the Python packages seaborn 0.10.1 [101] and Matplotlib 3.3.2 [95,102].

Venn diagrams were created using pyvenn (https://github.com/tctianchi/pyvenn) to illustrate overlap of significant differentially expressed proteins between 293 cells and PARP1cd cell lines.

All code was written in Python 3.8 and is available at https://github.com/MolecularBioinformatics/NADpools.

Model simulations

To simulate the effect of changes in NAD consumption and biosynthesis we constructed two mathematical models. To simulate the label integration in cell lines in a steady state situation, we created a mathematical model including a reaction for NAD consumption connected to NamPT and NMNAT to simulate the biosynthesis and consumption cycle. Only the major isotopologs were included, assuming instant labeling of glucose, Nam and PRPP. Competition between different isotopologs were simulated using competitive binding in random irreversible bimolecular reactions as described earlier [103]. In addition, ATP synthesis and degradation were simulated using mass action kinetics to be able to resemble the dynamic behavior of all major NAD isotopologs. The model is available at https://github.com/MolecularBioinformatics/NADpools. To simulate the individual enzyme kinetics, we removed the links between the reactions in the model by setting the respective substrates and products as external metabolites thus keeping them constant. This simulates the action of enzymes in isolation without flux balancing. Copasi 4.29 [104] was used to perform all simulations.

Statistical analyses

Statistical analyses were performed in RStudio: integrated development for *R* version 1.1.456 (RStudio, Inc., Boston, MA).

For all experiments except proteomics analyses, data were analyzed with ANOVA test. Prior to analysis, Levene's test was performed to confirm homogeneity of variance. Analysis of OCAR, ECAR and quantification of western blots did not meet the criteria and therefore were analyzed with a Welch's ANOVA. Between-group differences were then determined using Student's *t*-test, and Bonferronni corrections were applied to correct p-values for multiple testing.

For measurements of mitochondrial free NAD^+ using the biosensor, the differences between transfected and untransfected cells were evaluated with one-way Student's t-test.

References

1 Canto, C., Menzies, K. J. & Auwerx, J. NAD(+) metabolism and the control of energy homeostasis: A balancing act between mitochondria and the nucleus. *Cell Metab* **22**, 31-53, (2015).

2 Katsyuba, E., Romani, M., Hofer, D. & Auwerx, J. NAD(+) homeostasis in health and disease. *Nat Metab* **2**, 9-31, (2020).

3 Selles Vidal, L., Kelly, C. L., Mordaka, P. M. & Heap, J. T. Review of NAD(P)H-dependent oxidoreductases: Properties, engineering and application. *Biochim Biophys Acta Proteins Proteom* **1866**, 327-347, (2018).

4 Sultani, G., Samsudeen, A. F., Osborne, B. & Turner, N. NAD(+) : A key metabolic regulator with great therapeutic potential. *J Neuroendocrinol* **29**, (2017).

5 Yang, Y. & Sauve, A. A. NAD(+) metabolism: Bioenergetics, signaling and manipulation for therapy. *Biochim Biophys Acta* **1864**, 1787-1800, (2016).

6 Chini, E. N., Chini, C. C. S., Espindola Netto, J. M., de Oliveira, G. C. & van Schooten, W. The pharmacology of CD38/NADase: An emerging target in cancer and diseases of aging. *Trends Pharmacol Sci* **39**, 424-436, (2018).

7 Essuman, K. *et al.* The SARM1 toll/interleukin-1 receptor domain possesses intrinsic NAD(+) cleavage activity that promotes pathological axonal degeneration. *Neuron* **93**, 1334-1343 e1335, (2017).

8 Langelier, M. F., Eisemann, T., Riccio, A. A. & Pascal, J. M. PARP family enzymes: regulation and catalysis of the poly(ADP-ribose) posttranslational modification. *Curr Opin Struc Biol* **53**, 187-198, (2018).

9 Stromland, O. *et al.* Keeping the balance in NAD metabolism. *Biochem Soc Trans* **47**, 119-130, (2019).
10 Wang, Y. *et al.* An overview of Sirtuins as potential therapeutic target: Structure, function and modulators. *Eur J Med Chem* **161**, 48-77, (2019).
11 Ahel, D. *et al.* Poly(ADP-ribose)-dependent regulation of DNA repair by the chromatin remodeling enzyme ALC1. *Science* **325**, 1240-1243, (2009).
12 Chambon, P., Weill, J. D. & Mandel, P. Nicotinamide mononucleotide activation of new DNA-dependent polyadenylic acid synthesizing nuclear enzyme. *Biochem Biophys Res Commun* **11**, 39-43, (1963).
13 Croteau, D. L., Fang, E. F., Nilsen, H. & Bohr, V. A. NAD(+) in DNA repair and mitochondrial maintenance. *Cell Cycle* **16**, 491-492, (2017).
14 Durkacz, B. W., Omidiji, O., Gray, D. A. & Shall, S. (ADP-ribose)n participates in DNA excision repair. *Nature* **283**, 593-596, (1980).
15 Haince, J. F. *et al.* PARP1-dependent kinetics of recruitment of MRE11 and NBS1 proteins to multiple DNA damage sites. *J Biol Chem* **283**, 1197-1208, (2008).
16 Blander, G. & Guarente, L. The Sir2 family of protein deacetylases. *Annu Rev Biochem* **73**, 417-435, (2004).
17 Jackson, M. D. & Denu, J. M. Structural identification of 2'-and 3'-O-acetyl-ADP-ribose as novel metabolites derived from the Sir2 family of β-NAD+-dependent histone/protein deacetylases. *J Biol Chem* **277**, 18535-18544, (2002).
18 Haigis, M. C. & Sinclair, D. A. Mammalian sirtuins: biological insights and disease relevance. *Annu Rev Pathol* **5**, 253-295, (2010).
19 Imai, S., Armstrong, C. M., Kaeberlein, M. & Guarente, L. Transcriptional silencing and longevity protein Sir2 is an NAD-dependent histone deacetylase. *Nature* **403**, 795-800, (2000).
20 Michishita, E. *et al.* SIRT6 is a histone H3 lysine 9 deacetylase that modulates telomeric chromatin. *Nature* **452**, 492-U416, (2008).
21 Nakahata, Y. *et al.* The NAD(+)-dependent deacetylase SIRT1 modulates CLOCK-mediated chromatin remodeling and circadian control. *Cell* **134**, 329-340, (2008).
22 Nemoto, S., Fergusson, M. M. & Finkel, T. SIRT1 functionally interacts with the metabolic regulator and transcriptional coactivator PGC-1{alpha}. *J Biol Chem* **280**, 16456-16460, (2005).
23 Rodgers, J. T. *et al.* Nutrient control of glucose homeostasis through a complex of PGC-1alpha and SIRT1. *Nature* **434**, 113-118, (2005).
24 Schwer, B., Bunkenborg, J., Verdin, R. O., Andersen, J. S. & Verdin, E. Reversible lysine acetylation controls the activity of the mitochondrial enzyme acetyl-CoA synthetase 2. *Proc Natl Acad Sci U S A* **103**, 10224-10229, (2006).
25 Aarhus, R., Graeff, R. M., Dickey, D. M., Walseth, T. F. & Lee, H. C. ADP-ribosyl cyclase and CD38 catalyze the synthesis of a calcium-mobilizing metabolite from NADP. *J Biol Chem* **270**, 30327-30333, (1995).
26 De Flora, A., Franco, L., Guida, L., Bruzzone, S. & Zocchi, E. Ectocellular CD38-catalyzed synthesis and intracellular Ca(2+)-mobilizing activity of cyclic ADP-ribose. *Cell Biochem Biophys* **28**, 45-62, (1998).
27 Graeff, R. *et al.* Mechanism of cyclizing NAD to cyclic ADP-ribose by ADP-ribosyl cyclase and CD38. *J Biol Chem* **284**, 27629-27636, (2009).
28 Burgos, E. S. NAMPT in Regulated NAD Biosynthesis and its Pivotal Role in Human Metabolism. *Curr Med Chem* **18**, 1947-1961, (2011).

29 Burgos, E. S. & Schramm, V. L. Weak coupling of ATP hydrolysis to the chemical equilibrium of human nicotinamide phosphoribosyltransferase. *Biochemistry* **47**, 11086-11096, (2008).
30 Krehl, W. A., Teply, L. J., Sarma, P. S. & Elvehjem, C. A. Growth-retarding effect of corn in nicotinic acid-low rations and its counteraction by tryptophane. *Science* **101**, 489-490, (1945).
31 Preiss, J. & Handler, P. Biosynthesis of diphosphopyridine nucleotide I. Identification of intermediates. *J Biol Chem* **233**, 488-492, (1958).
32 Schutz, G. & Feigelson, P. Purification and properties of rat liver tryptophan oxygenase. *J Biol Chem* **247**, 5327-5332, (1972).
33 Imai, S. Nicotinamide Phosphoribosyltransferase (Nampt): A Link Between NAD Biology, Metabolism, and Diseases. *Current Pharmaceutical Design* **15**, 20-28, (2009).
34 Preiss, J. & Handler, P. Enzymatic synthesis of nicotinamide mononucleotide. *J Biol Chem* **225**, 759-770, (1957).
35 Bockwoldt, M. *et al.* Identification of evolutionary and kinetic drivers of NAD-dependent signaling. *Proc Natl Acad Sci U S A* **116**, 15957-15966, (2019).
36 Bieganowski, P. & Brenner, C. Discoveries of nicotinamide riboside as a nutrient and conserved NRK genes establish a Preiss-Handler independent route to NAD(+) in fungi and humans. *Cell* **117**, 495-502, (2004).
37 Magni, G., Amici, A., Emanuelli, M., Raffaelli, N. & Ruggieri, S. Enzymology of NAD+ synthesis. *Adv Enzymol Relat Areas Mol Biol* **73**, 135-182, xi, (1999).
38 Berger, F., Lau, C., Dahlmann, M. & Ziegler, M. Subcellular compartmentation and differential catalytic properties of the three human nicotinamide mononucleotide adenylyltransferase isoforms. *J Biol Chem* **280**, 36334-36341, (2005).
39 Araki, T., Sasaki, Y. & Milbrandt, J. Increased nuclear NAD biosynthesis and SIRT1 activation prevent axonal degeneration. *Science* **305**, 1010-1013, (2004).
40 Cambronne, X. A. & Kraus, W. L. Location, Location, Location: Compartmentalization of NAD(+) Synthesis and Functions in Mammalian Cells. *Trends Biochem Sci* **45**, 858-873, (2020).
41 Cambronne, X. A. *et al.* Biosensor reveals multiple sources for mitochondrial NAD(+). *Science* **352**, 1474-1477, (2016).
42 Ryu, K. W. *et al.* Metabolic regulation of transcription through compartmentalized NAD(+) biosynthesis. *Science* **360**, eaan5780, (2018).
43 Svoboda, P. *et al.* Nuclear transport of nicotinamide phosphoribosyltransferase is cell cycle-dependent in mammalian cells, and its inhibition slows cell growth. *J Biol Chem* **294**, 8676-8689, (2019).
44 Titov, D. V. *et al.* Complementation of mitochondrial electron transport chain by manipulation of the NAD(+)/NADH ratio. *Science* **352**, 231-235, (2016).
45 Pittelli, M. *et al.* Inhibition of nicotinamide phosphoribosyltransferase: cellular bioenergetics reveals a mitochondrial insensitive NAD pool. *J Biol Chem* **285**, 34106-34114, (2010).
46 Yang, H. *et al.* Nutrient-sensitive mitochondrial NAD+ levels dictate cell survival. *Cell* **130**, 1095-1107, (2007).
47 Davila, A. *et al.* Nicotinamide adenine dinucleotide is transported into mammalian mitochondria. *Elife* **7**, e33246, (2018).

48 Nikiforov, A., Dölle, C., Niere, M. & Ziegler, M. Pathways and subcellular compartmentation of NAD biosynthesis in human cells: from entry of extracellular precursors to mitochondrial NAD generation. *J Biol Chem* **286**, 21767-21778, (2011).
49 Kory, N. *et al.* MCART1/SLC25A51 is required for mitochondrial NAD transport. *Sci Adv* **6**, eabe5310, (2020).
50 Luongo, T. S. *et al.* SLC25A51 is a mammalian mitochondrial NAD+ transporter. *Nature*, 1-9, (2020).
51 Yamamoto, M. *et al.* Nmnat3 Is Dispensable in Mitochondrial NAD Level Maintenance In Vivo. *PLoS One* **11**, e0147037, (2016).
52 Dölle, C., Niere, M., Lohndal, E. & Ziegler, M. Visualization of subcellular NAD pools and intra-organellar protein localization by poly-ADP-ribose formation. *Cell Mol Life Sci* **67**, 433-443, (2010).
53 VanLinden, M. R., Niere, M., Nikiforov, A. A., Ziegler, M. & Dölle, C. Compartment-specific poly-ADP-ribose formation as a biosensor for subcellular NAD pools. *Methods Mol Biol* **1608**, 45-56, (2017).
54 Agrimi, G., Russo, A., Scarcia, P. & Palmieri, F. The human gene SLC25A17 encodes a peroxisomal transporter of coenzyme A, FAD and NAD(+). *Biochem J* **443**, 241-247, (2012).
55 Khan, N. A. *et al.* Effective treatment of mitochondrial myopathy by nicotinamide riboside, a vitamin B3. *EMBO Mol Med* **6**, 721-731, (2014).
56 Pirinen, E. *et al.* Niacin Cures Systemic NAD(+) Deficiency and Improves Muscle Performance in Adult-Onset Mitochondrial Myopathy. *Cell Metab* **31**, 1078-1090 e1075, (2020).
57 Gomes, A. P. *et al.* Declining NAD(+) induces a pseudohypoxic state disrupting nuclear-mitochondrial communication during aging. *Cell* **155**, 1624-1638, (2013).
58 Massudi, H. *et al.* Age-associated changes in oxidative stress and NAD+ metabolism in human tissue. *PLoS One* **7**, e42357, (2012).
59 Zhu, X.-H., Lu, M., Lee, B.-Y., Ugurbil, K. & Chen, W. In vivo NAD assay reveals the intracellular NAD contents and redox state in healthy human brain and their age dependences. *Proc Natl Acad Sci U S A* **112**, 2876-2881, (2015).
60 Liu, L. *et al.* Quantitative analysis of NAD synthesis-breakdown fluxes. *Cell Metabolism* **27**, 1067-1087, (2018).
61 Hasmann, M. & Schemainda, I. FK866, a highly specific noncompetitive inhibitor of nicotinamide phosphoribosyltransferase, represents a novel mechanism for induction of tumor cell apoptosis. *Cancer Res* **63**, 7436-7442, (2003).
62 Ratajczak, J. *et al.* NRK1 controls nicotinamide mononucleotide and nicotinamide riboside metabolism in mammalian cells. *Nat Commun* **7**, 13103, (2016).
63 Schuster, S. *et al.* FK866-induced NAMPT inhibition activates AMPK and downregulates mTOR signaling in hepatocarcinoma cells. *Biochem Biophys Res Commun* **458**, 334-340, (2015).
64 Tan, B. *et al.* Inhibition of nicotinamide phosphoribosyltransferase (NAMPT), an enzyme essential for NAD+ biosynthesis, leads to altered carbohydrate metabolism in cancer cells. *J Biol Chem* **290**, 15812-15824, (2015).
65 Skoge, R. H., Dölle, C. & Ziegler, M. Regulation of SIRT2-dependent alpha-tubulin deacetylation by cellular NAD levels. *DNA Repair (Amst)* **23**, 33-38, (2014).
66 Thakur, B. K. *et al.* Inhibition of NAMPT pathway by FK866 activates the function of p53 in HEK293T cells. *Biochem Biophys Res Commun* **424**, 371-377, (2012).

67 Niere, M., Kernstock, S., Koch-Nolte, F. & Ziegler, M. Functional localization of two poly(ADP-ribose)-degrading enzymes to the mitochondrial matrix. *Mol Cell Biol* **28**, 814-824, (2008).
68 VanLinden, M. R. *et al.* Subcellular distribution of NAD(+) between cytosol and mitochondria determines the metabolic profile of human cells. *J Biol Chem* **290**, 27644-27659, (2015).
69 Billington, R. A., Genazzani, A. A., Travelli, C. & Condorelli, F. NAD depletion by FK866 induces autophagy. *Autophagy* **4**, 385-387, (2008).
70 He, W., Newman, J. C., Wang, M. Z., Ho, L. & Verdin, E. Mitochondrial sirtuins: regulators of protein acylation and metabolism. *Trends Endocrinol Metab* **23**, 467-476, (2012).
71 Su, X. Y., Wellen, K. E. & Rabinowitz, J. D. Metabolic control of methylation and acetylation. *Curr Opin Chem Biol* **30**, 52-60, (2016).
72 Wellen, K. E. & Thompson, C. B. A two-way street: reciprocal regulation of metabolism and signalling. *Nat Rev Mol Cell Biol* **13**, 270-276, (2012).
73 North, B. J., Marshall, B. L., Borra, M. T., Denu, J. M. & Verdin, E. The human Sir2 ortholog, SIRT2, is an NAD(+)-dependent tubulin deacetylase. *Mol Cell* **11**, 437-444, (2003).
74 Park, J. A. *et al.* Deacetylation and methylation at histone H3 lysine 9 (H3K9) coordinate chromosome condensation during cell cycle progression. *Mol Cells* **31**, 343-349, (2011).
75 Salazar-Roa, M. & Malumbres, M. Fueling the Cell Division Cycle. *Trends Cell Biol* **27**, 69-81, (2017).
76 de Fries, R. & Mitsuhashi, M. Quantification of mitogen induced human lymphocyte proliferation: comparison of alamarBlue assay to 3H-thymidine incorporation assay. *J Clin Lab Anal* **9**, 89-95, (1995).
77 Schrader, M., Costello, J., Godinho, L. F. & Islinger, M. Peroxisome-mitochondria interplay and disease. *J Inherit Metab Dis* **38**, 681-702, (2015).
78 Sallin, O. *et al.* Semisynthetic biosensors for mapping cellular concentrations of nicotinamide adenine dinucleotides. *Elife* **7**, e32638, (2018).
79 Preiss, J. & Handler, P. Biosynthesis of diphosphopyridine nucleotide II. Enzymatic aspects. *J Biol Chem* **233**, 493-500, (1958).
80 Makarov, M. V., Harris, N. W., Rodrigues, M. & Migaud, M. E. Scalable syntheses of traceable ribosylated NAD(+) precursors. *Org Biomol Chem* **17**, 8716-8720, (2019).
81 Revollo, J. R., Grimm, A. A. & Imai, S. The regulation of nicotinamide adenine dinucleotide biosynthesis by Nampt/PBEF/visfatin in mammals. *Curr Opin Gastroenterol* **23**, 164-170, (2007).
82 Zhang, X. *et al.* Structural characterization of a human cytosolic NMN/NaMN adenylyltransferase and implication in human NAD biosynthesis. *J Biol Chem* **278**, 13503-13511, (2003).
83 Felici, R., Lapucci, A., Ramazzotti, M. & Chiarugi, A. Insight into molecular and functional properties of NMNAT3 reveals new hints of NAD homeostasis within human mitochondria. *PLoS One* **8**, e76938, (2013).
84 Pajuelo, D. *et al.* NAD(+) depletion triggers macrophage necroptosis, a cell death pathway exploited by Mycobacterium tuberculosis. *Cell Rep* **24**, 429-440, (2018).

85 Del Nagro, C., Xiao, Y., Rangell, L., Reichelt, M. & O'Brien, T. Depletion of the central metabolite NAD leads to oncosis-mediated cell death. *J Biol Chem* **289**, 35182-35192, (2014).
86 Kanehisa, M. & Goto, S. KEGG: kyoto encyclopedia of genes and genomes. *Nucleic Acids Res* **28**, 27-30, (2000).
87 Palmieri, F. The mitochondrial transporter family SLC25: identification, properties and physiopathology. *Mol Aspects Med* **34**, 465-484, (2013).
88 Ruprecht, J. J. & Kunji, E. R. S. The SLC25 mitochondrial carrier family: Structure and mechanism. *Trends Biochem Sci* **45**, 244-258, (2020).
89 Meier, S., Mjos, S. A., Joensen, H. & Grahl-Nielsen, O. Validation of a one-step extraction/methylation method for determination of fatty acids and cholesterol in marine tissues. *J Chromatogr A* **1104**, 291-298, (2006).
90 Mjos, S. A. Identification of fatty acids in gas chromatography by application of different temperature and pressure programs on a single capillary column. *J Chromatogr A* **1015**, 151-161, (2003).
91 Sciotto, C. & Mjos, S. A. Trans isomers of EPA and DHA in omega-3 products on the European market. *Lipids* **47**, 659-667, (2012).
92 Giskeodegard, G. F. *et al.* Metabolic markers in blood can separate prostate cancer from benign prostatic hyperplasia. *Br J Cancer* **113**, 1712-1719, (2015).
93 Dietze, J., van Pijkeren, A., Ziegler, M., Kwiatkowski, M. & Heiland, I. Natural isotope correction improves analysis of protein modification dynamics. *bioRxiv (November 01)*, doi: 10.1101/2020.1110.1131.361725 (2020).
94 Caswell, T. *et al.* matplotlib/matplotlib v3. 1.3 (2020). doi: 10.5281/zenodo.3633844
95 Hunter, J. D. Matplotlib: A 2D graphics environment. *Comput Sci Eng* **9**, 90-95, (2007).
96 Waskom, M. *et al.* mwaskom/seaborn: v0.10.0 (January 2020) (2020). doi: 10.5281/zenodo.3629446
97 Virtanen, P. *et al.* SciPy 1.0: fundamental algorithms for scientific computing in Python. *Nat Methods* **17**, 261-272, (2020).
98 Thompson, A. *et al.* Tandem mass tags: a novel quantification strategy for comparative analysis of complex protein mixtures by MS/MS. *Anal Chem* **75**, 1895-1904, (2003).
99 Kroksveen, A. C. *et al.* In-depth cerebrospinal fluid quantitative proteome and deglycoproteome analysis: Presenting a comprehensive picture of pathways and processes affected by multiple sclerosis. *J Proteome Res* **16**, 179-194, (2017).
100 Pedregosa, F. *et al.* Scikit-learn: Machine Learning in Python. *J Mach Learn Res* **12**, 2825-2830, (2011).
101 Waskom, M. *et al.* mwaskom/seaborn: v0. 10.1 (April 2020) (2020). doi: 10.5281/zenodo.3767070
102 Caswell, T. *et al.* matplotlib/matplotlib: REL: v3.3.2 (2020). doi: 10.5281/zenodo.4030140
103 Schäuble, S., Stavrum, A. K., Puntervoll, P., Schuster, S. & Heiland, I. Effect of substrate competition in kinetic models of metabolic networks. *FEBS Letters* **587**, 2818-2824, (2013).
104 Hoops, S. *et al.* COPASI--a COmplex PAthway SImulator. *Bioinformatics* **22**, 3067-3074, (2006).

Figure 1

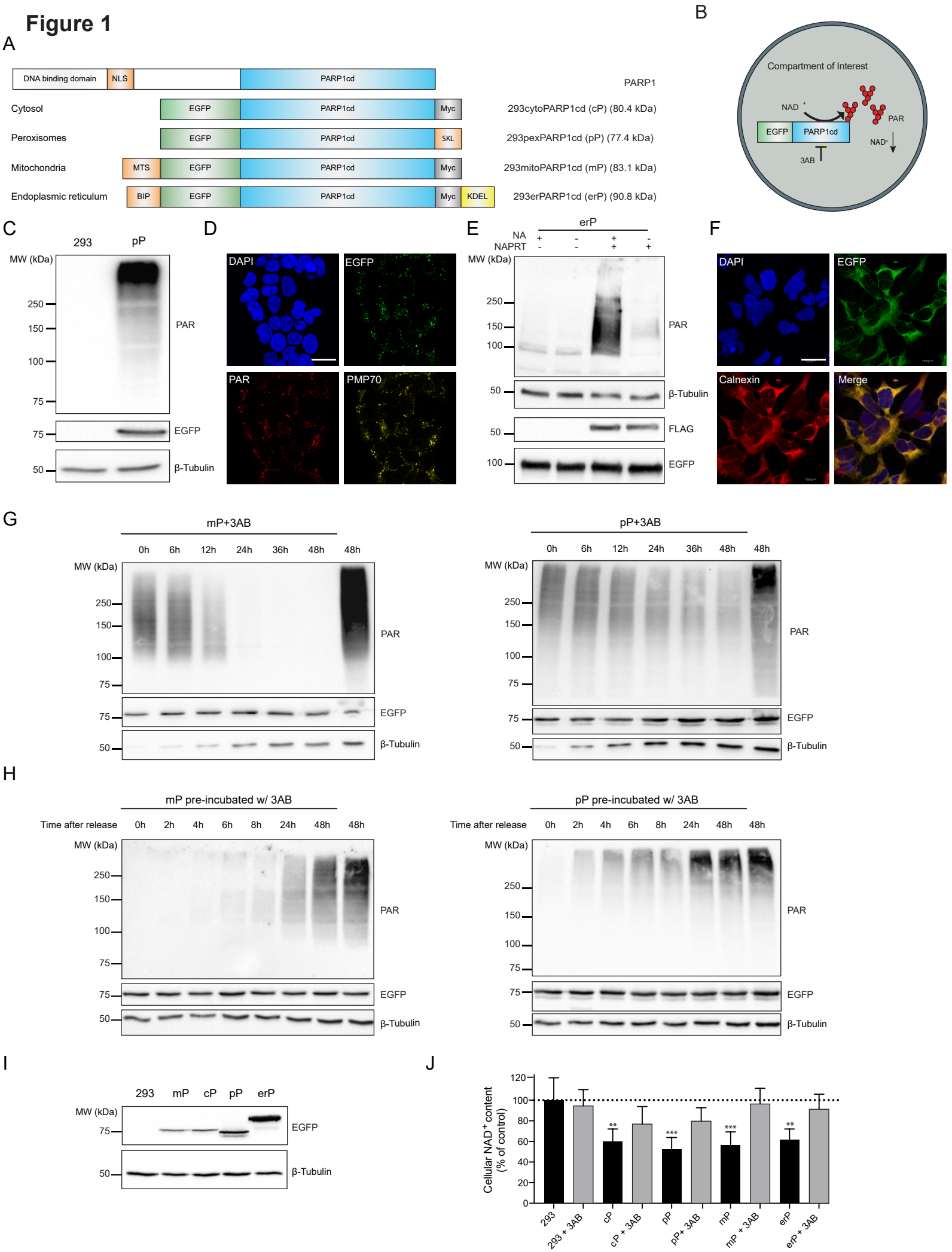
A
DNA binding domain
NLS
PARP1cd
PARP1
Cytosol
EGFP
PARP1cd
Myc
293cytoPARP1cd (cP) (80.4 kDa)
Peroxisomes
SKL
293pexPARP1cd (pP) (77.4 kDa)
Mitochondria
MTS
293mitoPARP1cd (mP) (83.1 kDa)
Endoplasmic reticulum
BIP
KDEL
293erPARP1cd (erP) (90.8 kDa)
B
Compartment of Interest
NAD+
PAR
NAD+
3AB
C
293
pP
MW (kDa)
250
150
100
75
50
PAR
EGFP
β-Tubulin
D
DAPI
EGFP
PAR
PMP70
E
erP
NA
NAPRT
MW (kDa)
250
150
100
50
100
PAR
β-Tubulin
FLAG
EGFP
F
DAPI
EGFP
Calnexin
Merge
G
mP+3AB
pP+3AB
0h
6h
12h
24h
36h
48h
48h
MW (kDa)
250
150
100
75
50
PAR
EGFP
β-Tubulin
H
mP pre-incubated w/ 3AB
pP pre-incubated w/ 3AB
Time after release
0h
2h
4h
6h
8h
24h
48h
48h
MW (kDa)
250
150
100
75
50
PAR
EGFP
β-Tubulin
I
293
mP
cP
pP
erP
MW (kDa)
75
50
EGFP
β-Tubulin
J
Cellular NAD+ content (% of control)
120
100
80
60
40
20
0
**
***
***
**
293
293 + 3AB
cP
cP + 3AB
pP
pP+ 3AB
mP
mP + 3AB
erP
erP + 3AB

Figure 1: PARP1cd expression decreases cellular NAD^+ content by ~40%, irrespective of the subcellular compartment targeted

(A) Schematic illustration of Poly-ADP-ribose polymerase 1 (PARP1) and PARP1 catalytic domain (PARP1cd) fusion proteins targeted to the cytosol, the peroxisomes, the mitochondria, or the endoplasmic reticulum (ER). BIP - ER targeting signal, EGFP - enhanced green fluorescent protein, KDEL – ER retention sequence, MTS - Mitochondrial targeting signal, Myc - myc-tag, NLS - nuclear localization signal, SKL-peroxisomal targeting sequence.

(B) Constitutive expression of PARP1cd fusion proteins in the compartment of interest results in the generation of poly-ADP-ribose (PAR). PAR formation can be modulated by the PARP inhibitor 3-aminobenzamide (3AB).

(C) PAR immunoblot analysis of lysates from parental 293 and stably transfected 293pexPARP1cd (pP) cells. Expression of the fusion protein was confirmed by detection of the EGFP tag, while β-tubulin served as a loading control. Results shown are representative of four repetitions.

(D) Confocal fluorescence micrographs of stably transfected 293pexPARP1cd cells. Nuclei were stained with DAPI, the fusion protein was detected by its EGFP tag, visualization of PAR was achieved by indirect immunocytochemistry using the PAR (10H) antibody, and peroxisomes were detected using the peroxisomal marker protein PMP70. Scale bar 20 µm.

(E) PAR immunoblot analysis of stably transfected 293erPARP1cd (erP) cells with and without transient overexpression of Nicotinic acid phosphoribosyltransferase (NAPRT) and nicotinic acid (NA) supplementation. Expression of the erPARP1cd fusion protein was confirmed by detection of the EGFP tag, while transient overexpression of NAPRT was detected by its FLAG-tag. β-tubulin served as a loading control. Results shown are representative of three repetitions.

(F) Confocal fluorescence micrographs of stably transfected 293erPARP1cd cells. Nuclei were stained with DAPI, the fusion protein was detected by its EGFP tag, and the ER was detected using the ER maker protein Calnexin. Scale bar 20 µm.

(G) PAR immunoblot analyses of cell lysates from 293mitoPARP1cd (mP) cells, and 293pexPARP1cd cells (pP) incubated in the presence of 3AB (1 mM) for up to 48h. Equal sample volumes were loaded. Expression of the recombinant protein was confirmed by detection of the EGFP tag, while β-tubulin served as a loading control. Results shown are representative of four repetitions.

(H) PAR immunoblot analyses of cell lysates from 293mitoPARP1cd cells (mP), and 293pexPARP1cd cells (pP). Cells were incubated in the presence of 3AB (1 mM) for 48h. Upon washout, the cells were cultured in the absence of 3AB for up to 48h. Expression of the recombinant protein was confirmed by detection of the EGFP tag, while β-tubulin served as a loading control. Results shown are representative of four repetitions.

(I) Immunoblot analysis of lysates from parental 293 cells and stably transfected PARP1cd cell lines reveals differences in the expression of the PARP1cd fusion proteins as detected by their EGFP tags. β-Tubulin served as a loading control. Results shown are representative of five repetitions.

Total cellular NAD^+ content in parental 293 cells and stably transfected PARP1cd cell lines as determined by methanol extraction and LC-MS analysis. Measurements were performed in presence or absence of 3AB (1 mM, 48h). Results were normalized to

protein content and data are represented relative to parental 293 cells as mean ± SD where n = 3. *p ≤ 0.05, **p ≤ 0.01, ***p ≤ 0.001 (student's t-test).

mP - 293mitoPARP1cd, pP – 293pexPARP1cd, cP – 293cytoPARP1cd, erP – 293erPARP1cd.

Figure 2

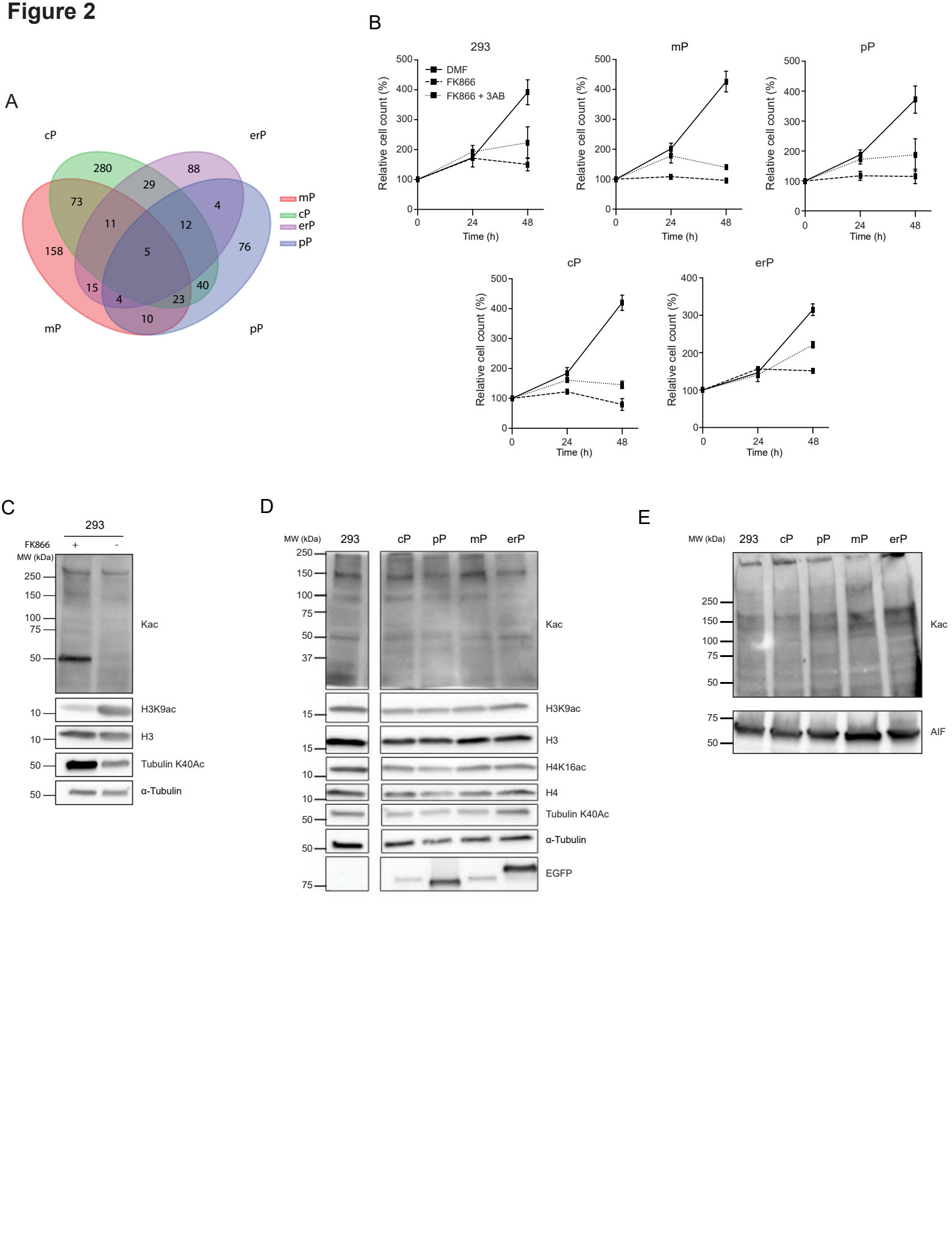
A
cP
erP
mP
pP
280
88
29
73
4
11
12
158
5
76
15
40
4
23
10
B
293
mP
pP
cP
erP
DMF
FK866
FK866 + 3AB
Relative cell count (%)
Time (h)
C
293
FK866
+
-
MW (kDa)
250
150
100
75
50
Kac
10
H3K9ac
H3
Tubulin K40Ac
α-Tubulin
D
MW (kDa)
293
cP
pP
mP
erP
250
150
100
75
50
37
Kac
15
H3K9ac
H3
H4K16ac
H4
Tubulin K40Ac
α-Tubulin
EGFP
E
MW (kDa)
293
cP
pP
mP
erP
250
150
100
75
50
Kac
AIF

Figure 2: Chronic NAD^+ depletion is tolerated surprisingly well by human cells

A) Venn diagram of differential protein abundance in PARP1cd cell lines in comparison to 293 cells ($p<0.001$)

B) Cell proliferation in parental 293 cells and stably transfected PARP1cd cell lines in the absence or presence of the NamPT inhibitor FK866 (2 µM) or its solvent DMF. Additionally, cells were incubated in the presence of both FK866 (2 µM) and the PARP inhibitor 3-aminobenzamide (3AB, 1 mM). Data are presented as means ± SD where n = 3.

C) Overall lysine (Kac), tubulin and histone acetylation as determined by immunoblot analysis of lysates from parental 293 cells incubated in the presence or absence of the NamPT inhibitor FK866 (2 µM). Results shown are representative of three independent repetitions.

D) Overall lysine (Kac), tubulin and histone acetylation as determined by immunoblot analysis of lysates from parental 293 cells and stably transfected PARP1cd cell lines. Expression of the fusion proteins was confirmed by detection of the EGFP tags, while α-tubulin served as a loading control. Results shown are representative of three independent repetitions.

E) Mitochondrial lysine acetylation (Kac) as determined by immunoblot analysis of mitochondrial extracts from parental 293 cells and stably transfected PARP1cd cell lines. The mitochondrial protein apoptosis-inducing factor (AIF) served as a loading control. Results shown are representative of three independent repetitions.

mP - 293mitoPARP1cd, pP – 293pexPARP1cd, cP – 293cytoPARP1cd, erP – 293erPARP1cd.

Figure 3

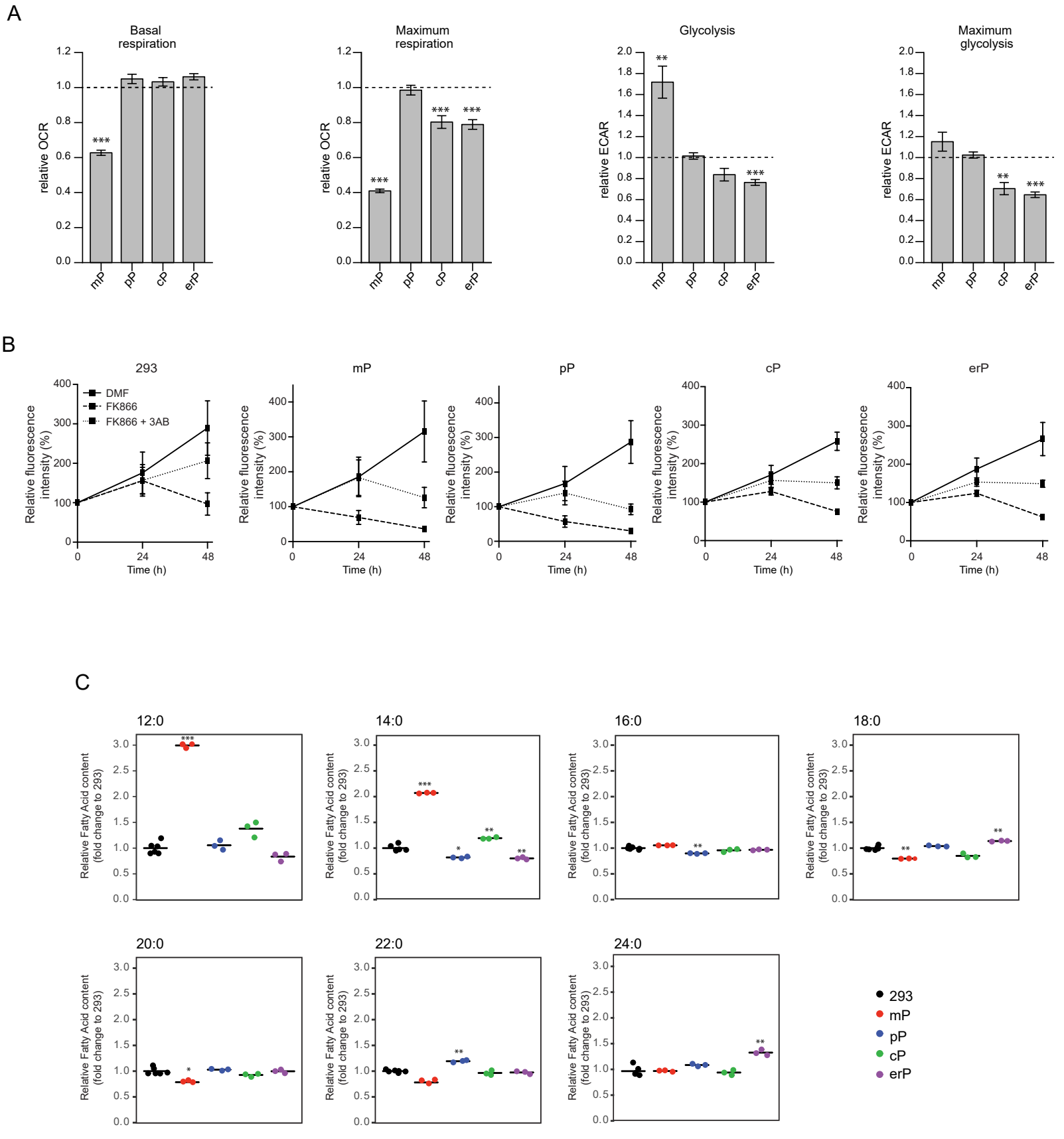
A
Basal respiration
relative OCR
Maximum respiration
relative OCR
Glycolysis
relative ECAR
Maximum glycolysis
relative ECAR
mP
pP
cP
erP
B
293
mP
pP
cP
erP
DMF
FK866
FK866 + 3AB
Relative fluorescence intensity (%)
Time (h)
C
12:0
14:0
16:0
18:0
20:0
22:0
24:0
Relative Fatty Acid content (fold change to 293)
293
mP
pP
cP
erP

Figure 3: Direct mitochondrial NAD^+ depletion affects bioenergetics

A) Activity and integrity of mitochondrial respiration in terms of oxygen consumption rate (OCR), and glycolysis in terms of extracellular acidification rate (ECAR) in stably transfected PARP1cd cell lines compared to parental 293 cells as determined by extracellular flux analysis. Data are presented relative to parental 293 cells as mean ± SEM where n = 3. *p ≤ 0.05, **p ≤ 0.01, ***p ≤ 0.001 (Student's t-test).

B) Activity of mitochondrial NAD-dependent dehydrogenases as measured by resazurin assay in parental 293 cells and stably transfected PARP1cd cell lines in the absence or presence of the NamPT inhibitor FK866 (2 µM) or its solvent DMF. Additionally, cells were incubated in the presence of both FK866 (2 µM) and the PARP inhibitor 3-aminobenzamide (3AB, 1 mM). Data are presented as mean ± SD where n = 3.

C) Relative cellular abundance of fully saturated fatty acids in stably transfected PARP1cd cell lines compared to parental 293 cells as determined by gas chromatography. The abundance of each fatty acid is normalized to total fatty acid content.

D) Data are presented as mean ± SD where n ≥ 3. *p ≤ 0.05, **p ≤ 0.01, ***p ≤ 0.001 (Student's t-test).

mP - 293mitoPARP1cd, pP – 293pexPARP1cd, cP – 293cytoPARP1cd, erP – 293erPARP1cd.

Figure 4

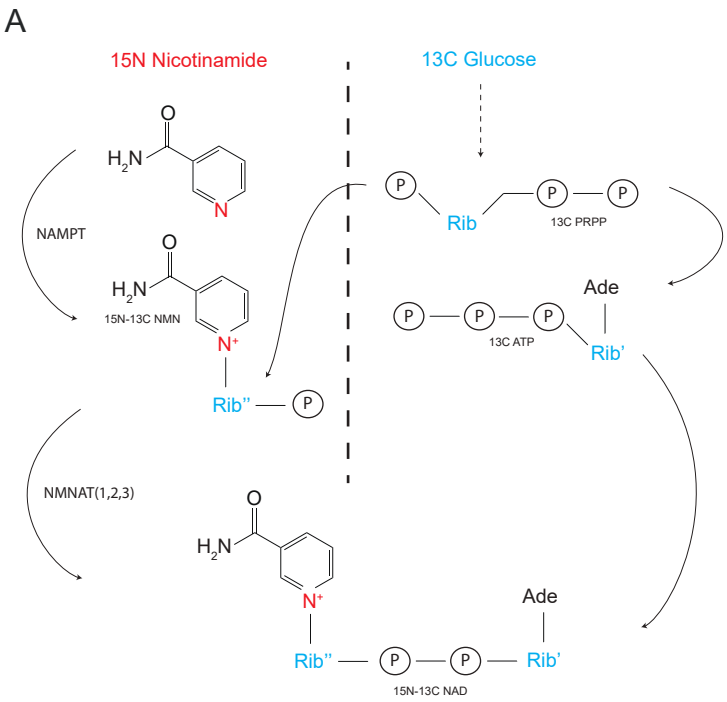

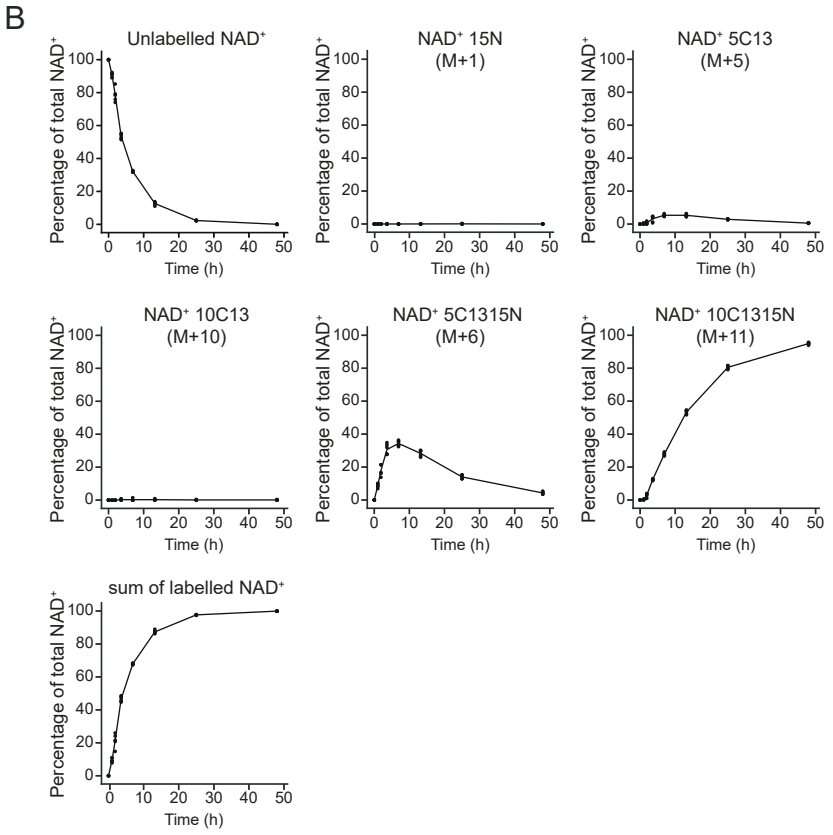

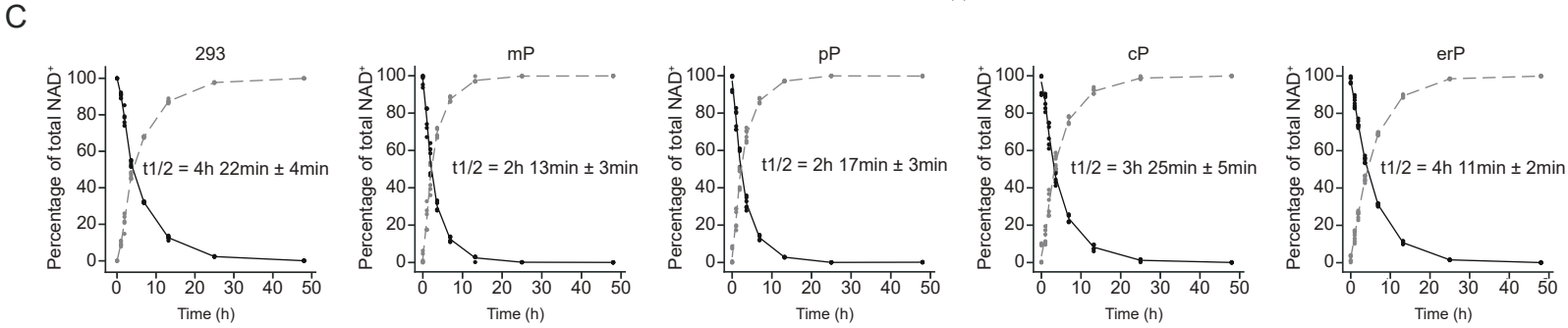

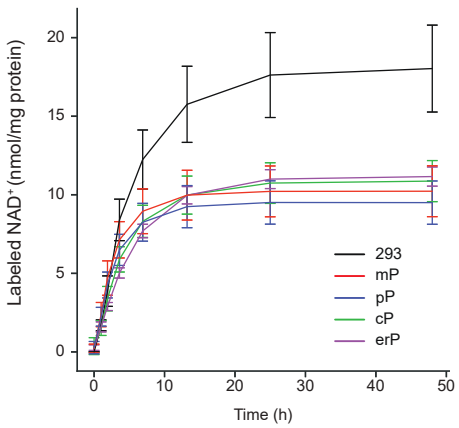

	Turnover (nmol/h·mg protein)
293	3.1 ± 0.2
mP	3.2 ± 0.2
pP	2.8 ± 0.1
cP	2.2 ± 0.1
erP	1.8 ± 0.1

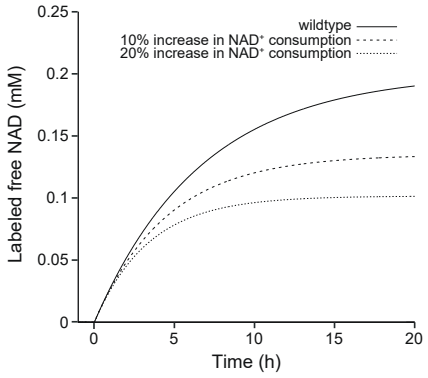

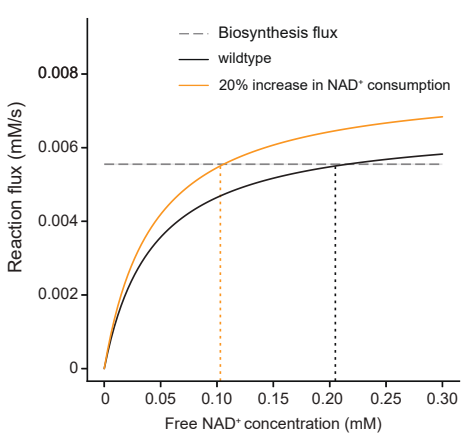

Figure 4: Total cellular NAD^+ turnover is not increased by PARP1cd overexpression

A) Schematic representation of the labelling approach used in this study. Cells were incubated with isotopically labelled nicotinamide (15N, red) or glucose (13C, blue), allowing for labelling on both the Nam-moiety and the ribose-moieties.

B) The time-dependent appearance of labelled isotopologs is accompanied by the disappearance of unlabeled NAD^+ upon incubation of parental 293 cells in the presence of isotopically labelled nicotinamide (15N), and glucose (13C) where n = 6.

C) Half-life of NAD^+ in parental 293 and PARP1cd cell lines in terms of the time-dependent appearance of the sum of labelled NAD^+ species (dashed line) and respective disappearance of unlabeled NAD^+ (solid line) where n = 6.

D) Time courses for NAD^+ labelling in parental 293 and PARP1cd cell lines normalized to steady state NAD^+ concentrations per protein. Data are presented as means ± SD where $n \geq 6$. The table lists the estimated NAD turnover.

E) Simulations of NAD^+ labelling time courses using a minimal mathematical model of NAD^+ biosynthesis and consumption. PARP1cd overexpression was modelled by increasing the maximal velocity of NAD^+ consumption while keeping the maximal velocity of NAD^+ biosynthesis constant.

F) Demand-supply model showing the dynamics of NAD^+-consumption and NAD^+-biosynthesis in isolated enzymes. To achieve steady state both processes have to balance each other. The intersection therefore represents the theoretical steady state concentration of NAD, demonstrating the kinetic balancing effect that leads to decreased NAD concentration upon overexpression of PARP1cd.
mP - 293mitoPARP1cd, pP – 293pexPARP1cd, cP – 293cytoPARP1cd, erP – 293erPARP1cd

Figure 5

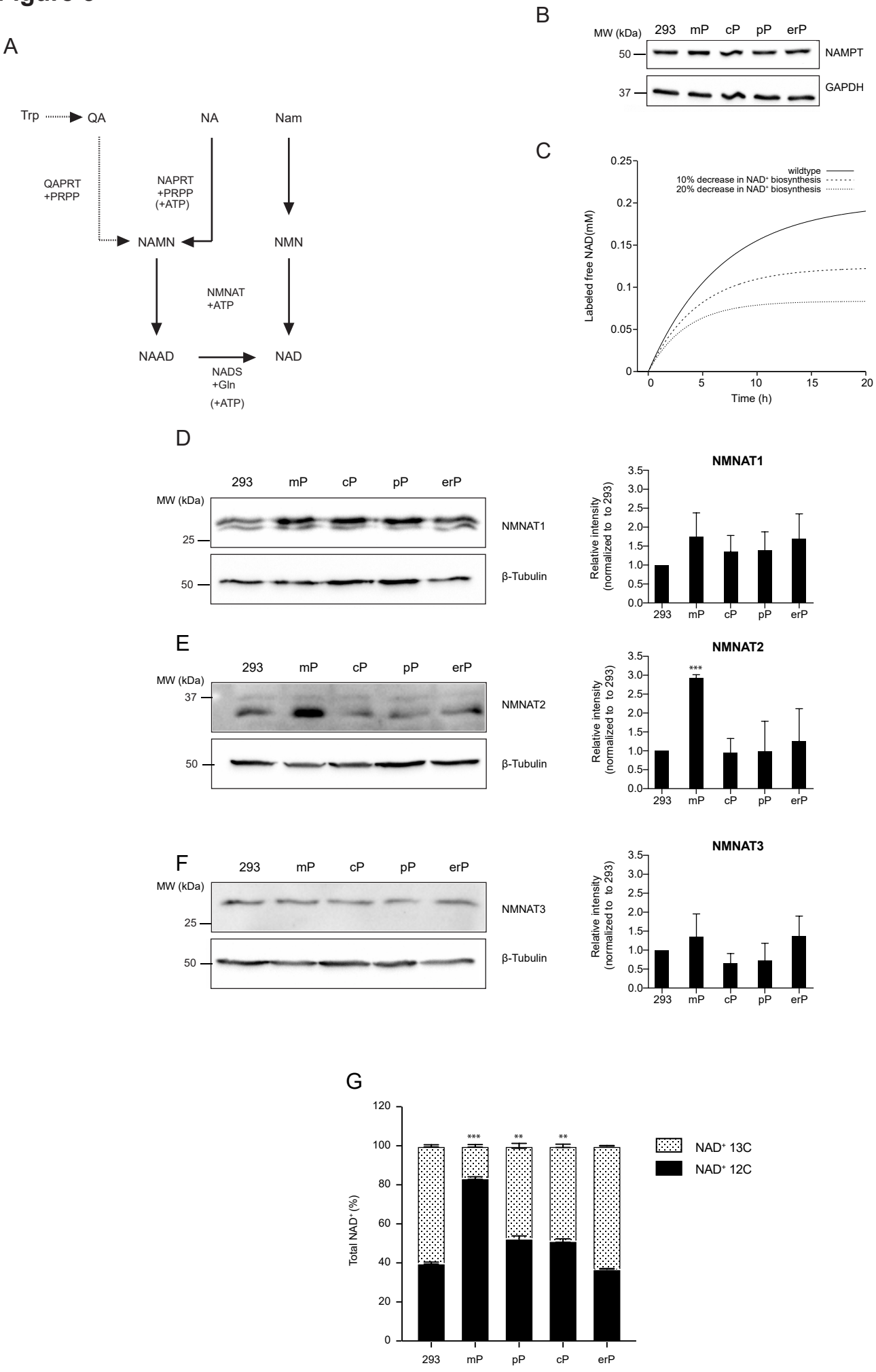
A
Trp
QA
NA
Nam
QAPRT
+PRPP
NAPRT
+PRPP
(+ATP)
NAMN
NMN
NMNAT
+ATP
NAAD
NAD
NADS
+Gln
(+ATP)
B
MW (kDa)
293
mP
cP
pP
erP
50
NAMPT
37
GAPDH
C
wildtype
10% decrease in NAD+ biosynthesis
20% decrease in NAD+ biosynthesis
Labeled free NAD(mM)
Time (h)
D
MW (kDa)
25
50
NMNAT1
β-Tubulin
NMNAT1
Relative intensity
(normalized to 293)
E
37
NMNAT2
NMNAT2
***
F
NMNAT3
NMNAT3
G
Total NAD+ (%)
**
NAD+ 13C
NAD+ 12C

Figure 5: Stable NAD^+ biosynthesis kinetically limits NAD^+ consumption

A) Schematic representation of the *de novo*, Preiss-handler and salvage NAD biosynthetic pathways.
B) NamPT Immunoblot analysis of lysates from parental 293 cells and stably transfected PARP cell lines. GAPDH served as a loading control. Results shown are representative of four repetitions.
C) Simulations of NAD^+ labelling time courses using a minimal mathematical model of NAD^+ biosynthesis and consumption, demonstrating the effect of NAD^+ biosynthesis decrease while keeping the maximal velocity of NAD^+ consumption constant
D) NMNAT1 protein expression in PARP1cd cell lines compared to parental 293 cells as analyzed by western blotting. β -tubulin served as a loading control. Data are presented as mean ± SD where n = 4.
E) NMNAT2 protein expression in PARP1cd cell lines compared to parental 293 cells as analyzed by western blotting. β -tubulin served as a loading control. Data are presented as mean ± SD where n = 4. *$p \leq 0.05$, **$p \leq 0.01$, ***$p \leq 0.001$ (Student's t-test).
F) NMNAT3 protein expression in PARP1cd cell lines compared to parental 293 cells as analyzed by western blotting. β -tubulin served as a loading control. Data are presented as mean ± SD where n = 4.
G) Distribution of NAD labeling following 48 h incubation of parental 293 cells and stably transfected PARP1cd cell lines in the presence of NA 13C.
mP - 293mitoPARP1cd, pP – 293pexPARP1cd, cP – 293cytoPARP1cd, erP – 293erPARP1cd

Figure 6

A

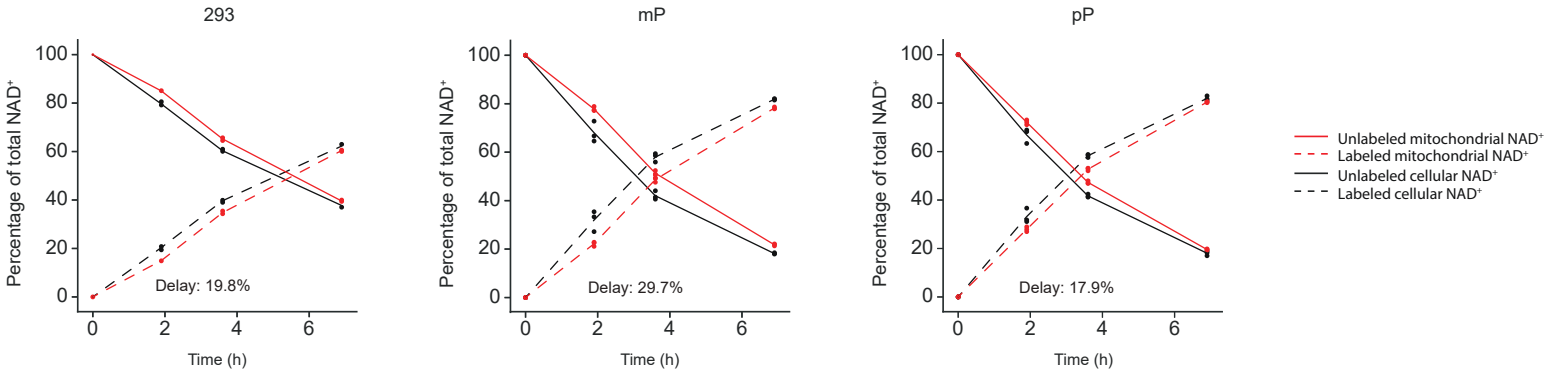

B

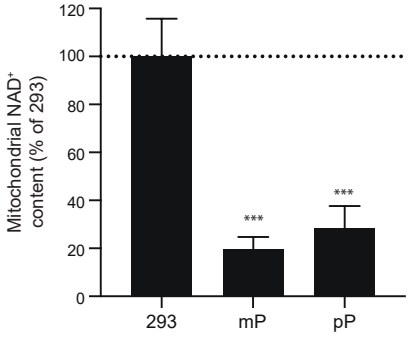

C

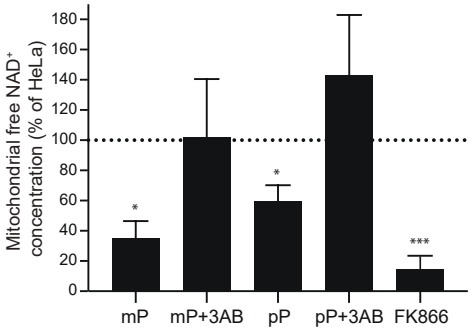

D

	Mitochondrial turnover (fmol/(h/cell))	Cell w/o mitochondria turnover (fmol/(h/cell))
293	0.21	0.50
mP	0.06	0.60
pP	0.10	0.53

Figure 6: Direct, but not indirect depletion of mitochondrial NAD^+ is detrimental to cellular homeostasis

A) Time-dependent appearance of the sum of labelled NAD^+ species (dashed line) and disappearance of unlabeled NAD^+ (solid line) in whole cell lysate (WCL, black) and mitochondria (red) upon incubation in the presence of 15N nicotinamide and 13C glucose. Delays are presented as the difference between mitochondrial and extramitochondrial (total minus mitochondrial) half-lives relative to the half-life of extramitochondrial NAD^+. Experimental data where $n \geq 3$. mP - 293mitoPARP1cd, pP – 293pexPARP1cd.

B) Mitochondrial NAD^+ content in parental 293 cells and stably transfected 293mitoPARP1cd (mP) and 293 pexPARP1cd (pP) cell lines as determined by mitochondrial isolation followed by methanol extraction and LC-MS analysis. Results were normalized to protein content and data are represented relative to parental 293 cells as mean ± SD where $n = 3$. *$p \leq 0.05$, **$p \leq 0.01$, ***$p \leq 0.001$ (Student's t-test).

C) Free mitochondrial NAD^+ concentration in untreated HeLa cells, as well as upon transient transfection with red mitoPARP1cd (mP) and pexPARP1cd (pP) constructs. NAD^+ concentrations were calculated from sensor (488/405 nm)/control (488/405 nm) fluorescence ratios determined by flow cytometry (see Figure S6). Measurements were performed in presence or absence of 3-aminobenzamide (3AB, 1 mM, 48h), and incubation of HeLa cells with FK866 (2 µM) served as a positive control. Results are represented relative to untransfected control cells as mean ± SD where $n \geq 3$.

D) The mitochondrial and cytosolic NAD^+ turnover per cell as calculated for parental 293 cells, as well as stably transfected transfected 293mitoPARP1cd (mP) and 293 pexPARP1cd (pP) cell lines taking into account the cellular NAD^+ distribution.

Figure 7

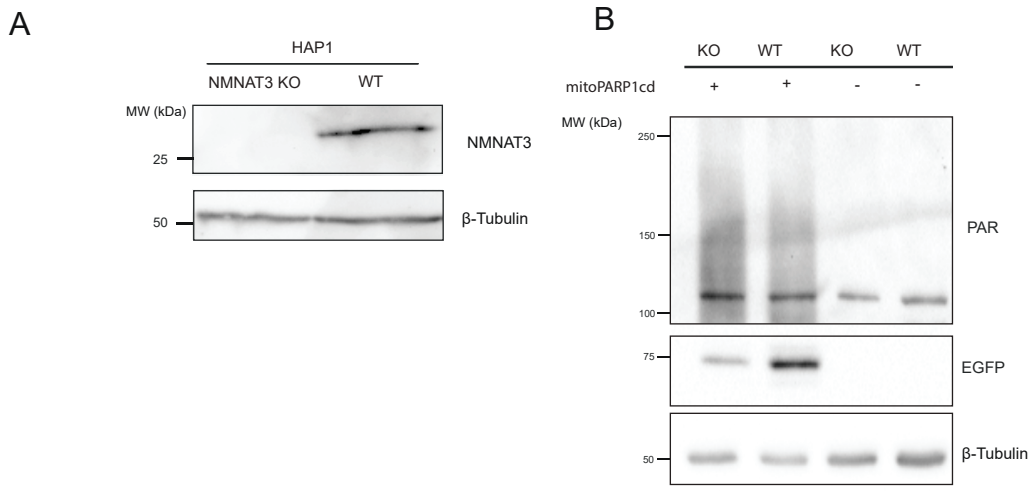
A
HAP1
NMNAT3 KO
WT
MW (kDa)
25
50
NMNAT3
β-Tubulin
B
KO
WT
KO
WT
mitoPARP1cd
+
+
-
-
MW (kDa)
250
150
100
75
50
PAR
EGFP
β-Tubulin

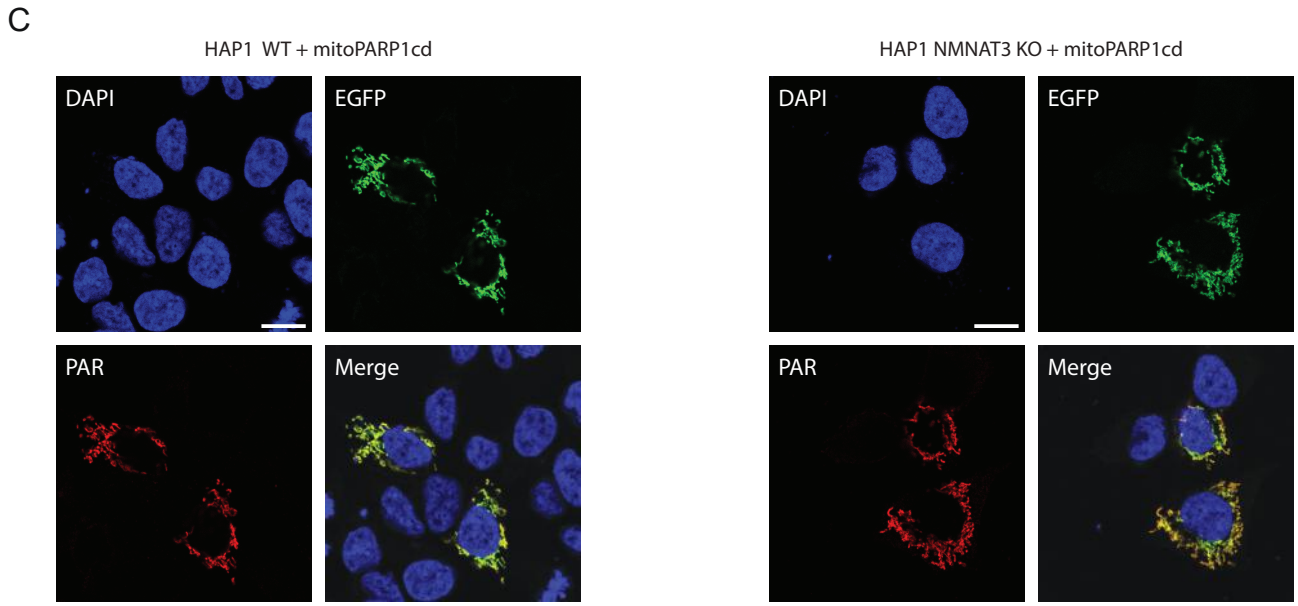
C
HAP1 WT + mitoPARP1cd
HAP1 NMNAT3 KO + mitoPARP1cd
DAPI
EGFP
PAR
Merge
DAPI
EGFP
PAR
Merge

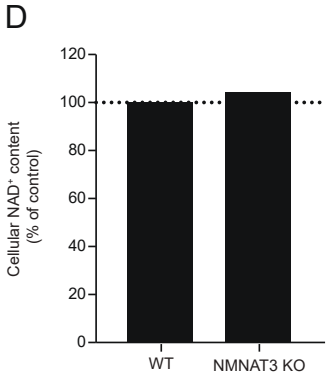
D
Cellular NAD⁺ content
(% of control)
120
100
80
60
40
20
0
WT
NMNAT3 KO

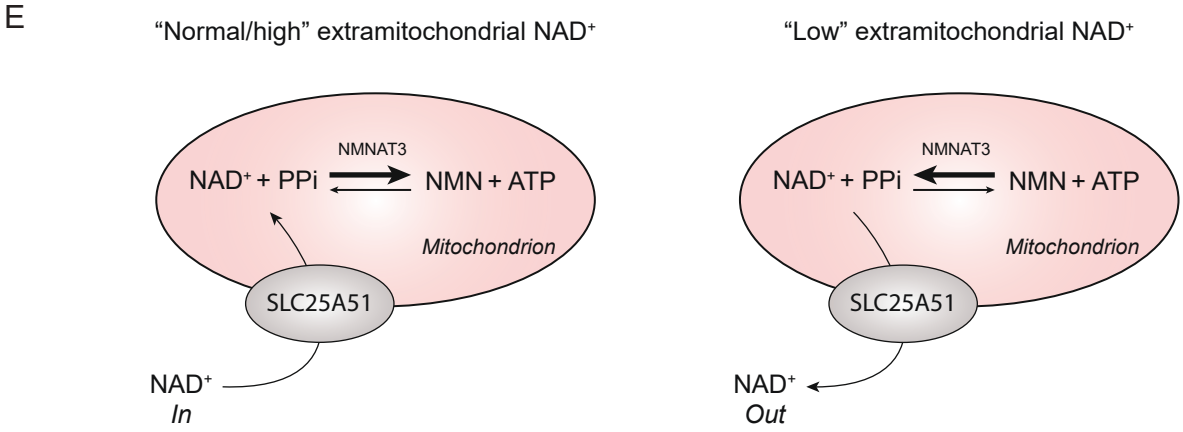
E
"Normal/high" extramitochondrial NAD⁺
"Low" extramitochondrial NAD⁺
NMNAT3
NAD⁺ + PPi
NMN + ATP
Mitochondrion
SLC25A51
NAD⁺
In
NMNAT3
NAD⁺ + PPi
NMN + ATP
Mitochondrion
SLC25A51
NAD⁺
Out

Figure 7: NMNAT3 is not required for mitochondrial NAD^+ generation

A) Immunoblot analysis of NMNAT3 expression in HAP1 wild type (WT) and *NMNAT3*$^{-/-}$ cells (NMNAT3 KO) cells. β-tubulin served as a loading control.
B) PAR immunoblot analysis of lysates from HAP1 wild type (WT) and *NMNAT3*$^{-/-}$ cells (NMNAT3 KO) cells transiently transfected with mitoPARP1cd. Expression of the mitoPARP1cd fusion protein was confirmed by its intrinsic green fluorescence, while β-tubulin served as a loading control.
C) Confocal fluorescence micrographs of HAP1 wild type (WT) and *NMNAT3*$^{-/-}$ cells (NMNAT3 KO) cells transiently transfected with mitoPARP1cd. Nuclei were stained with DAPI, the fusion protein was detected by its intrinsic green fluorescence, and visualization of PAR was achieved by indirect immunocytochemistry using the PAR (10H) antibody. Scale bar 20 μm.
D) Determination of the total cellular NAD^+ content in HAP1 wild type (WT) and *NMNAT3*$^{-/-}$ cells (NMNAT3 KO) cells by methanol extraction and LC-MS analysis. Results were normalized to protein content and data are represented relative to HAP1 WT cells as mean ± SD where n = 3.
E) Schematic representation of a proposed model for the collaboration of SLC25A51 and NMNAT3 in situations of normal/high and low extramitochondrial NAD.

Figures

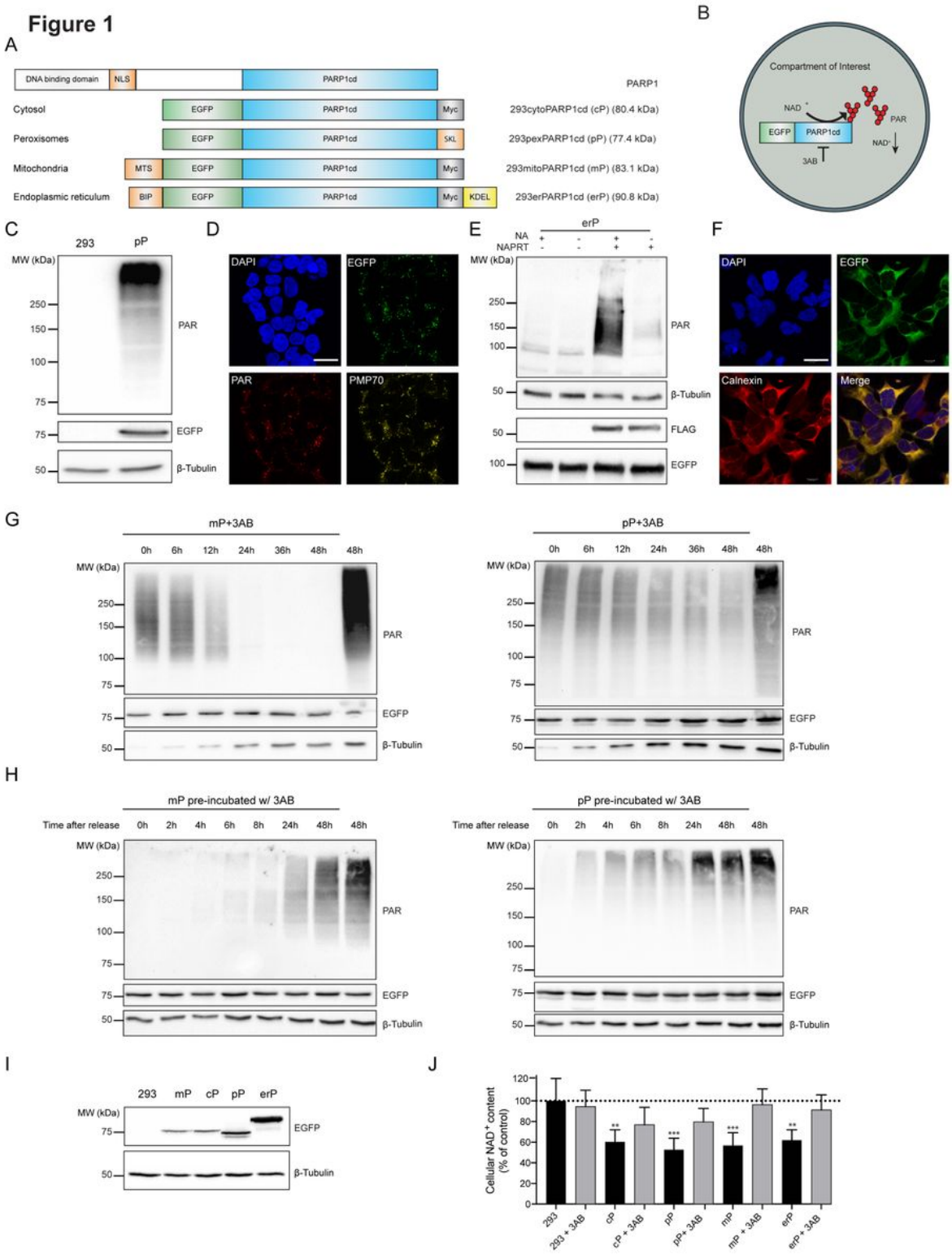

Figure 1

PARP1cd expression decreases cellular NAD+ content by ~40%, irrespective of the subcellular compartment targeted (A) Schematic illustration of Poly-ADP-ribose polymerase 1 (PARP1) and PARP1 catalytic domain (PARP1cd) fusion proteins targeted to the cytosol, the peroxisomes, the mitochondria, or

the endoplasmic reticulum (ER). BIP - ER targeting signal, EGFP - enhanced green fluorescent protein, KDEL – ER retention sequence, MTS - Mitochondrial targeting signal, Myc - myc-tag, NLS - nuclear localization signal, SKLperoxisomal targeting sequence. (B) Constitutive expression of PARP1cd fusion proteins in the compartment of interest results in the generation of poly-ADP-ribose (PAR). PAR formation can be modulated by the PARP inhibitor 3-aminobenzamide (3AB). (C) PAR immunoblot analysis of lysates from parental 293 and stably transfected 293pexPARP1cd (pP) cells. Expression of the fusion protein was confirmed by detection of the EGFP tag, while β-tubulin served as a loading control. Results shown are representative of four repetitions. (D) Confocal fluorescence micrographs of stably transfected 293pexPARP1cd cells. Nuclei were stained with DAPI, the fusion protein was detected by its EGFP tag, visualization of PAR was achieved by indirect immunocytochemistry using the PAR (10H) antibody, and peroxisomes were detected using the peroxisomal marker protein PMP70. Scale bar 20 μm. (E) PAR immunoblot analysis of stably transfected 293erPARP1cd (erP) cells with and without transient overexpression of Nicotinic acid phosphoribosyltransferase (NAPRT) and nicotinic acid (NA) supplementation. Expression of the erPARP1cd fusion protein was confirmed by detection of the EGFP tag, while transient overexpression of NAPRT was detected by its FLAG-tag. β-tubulin served as a loading control. Results shown are representative of three repetitions. (F) Confocal fluorescence micrographs of stably transfected 293erPARP1cd cells. Nuclei were stained with DAPI, the fusion protein was detected by its EGFP tag, and the ER was detected using the ER maker protein Calnexin. Scale bar 20 μm. (G) PAR immunoblot analyses of cell lysates from 293mitoPARP1cd (mP) cells, and 293pexPARP1cd cells (pP) incubated in the presence of 3AB (1 mM) for up to 48h. Equal sample volumes were loaded. Expression of the recombinant protein was confirmed by detection of the EGFP tag, while β-tubulin served as a loading control. Results shown are representative of four repetitions. (H) PAR immunoblot analyses of cell lysates from 293mitoPARP1cd cells (mP), and 293pexPARP1cd cells (pP). Cells were incubated in the presence of 3AB (1 mM) for 48h. Upon washout, the cells were cultured in the absence of 3AB for up to 48h. Expression of the recombinant protein was confirmed by detection of the EGFP tag, while β-tubulin served as a loading control. Results shown are representative of four repetitions. (I) Immunoblot analysis of lysates from parental 293 cells and stably transfected PARP1cd cell lines reveals differences in the expression of the PARP1cd fusion proteins as detected by their EGFP tags. β-Tubulin served as a loading control. Results shown are representative of five repetitions. Total cellular NAD+ content in parental 293 cells and stably transfected PARP1cd cell lines as determined by methanol extraction and LC-MS analysis. Measurements were performed in presence or absence of 3AB (1 mM, 48h). Results were normalized to protein content and data are represented relative to parental 293 cells as mean ± SD where n = 3. *$p \leq 0.05$, **$p \leq 0.01$, ***$p \leq 0.001$ (student's t-test). mP - 293mitoPARP1cd, pP – 293pexPARP1cd, cP – 293cytoPARP1cd, erP – 293erPARP1cd.

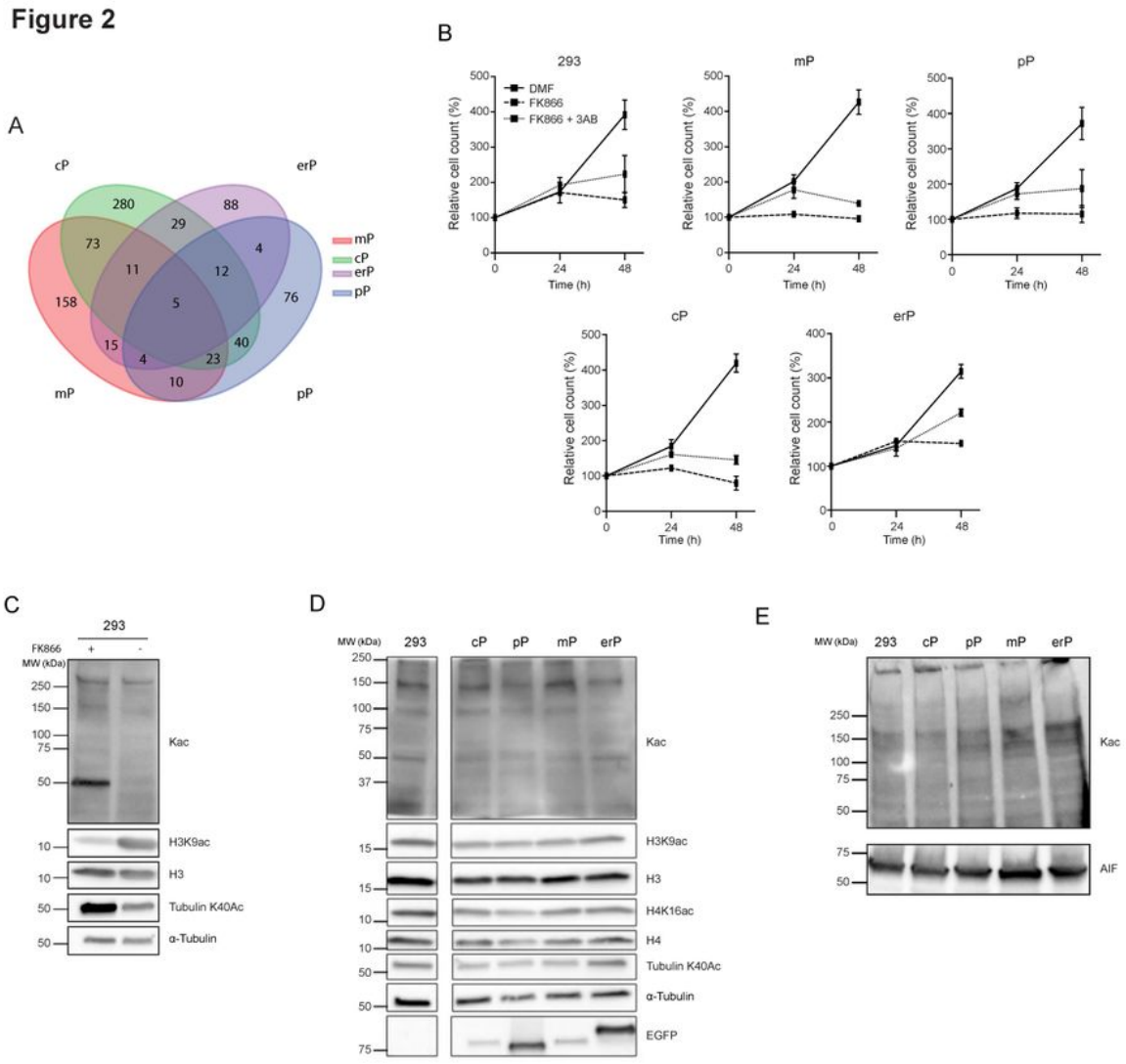

Figure 2

Chronic NAD+ depletion is tolerated surprisingly well by human cells A) Venn diagram of differential protein abundance in PARP1cd cell lines in comparison to 293 cells ($p<0.001$) B) Cell proliferation in parental 293 cells and stably transfected PARP1cd cell lines in the absence or presence of the NamPT inhibitor FK866 (2 µM) or its solvent DMF. Additionally, cells were incubated in the presence of both FK866 (2 µM) and the PARP inhibitor 3-aminobenzamide (3AB, 1 mM). Data are presented as means ±

SD where n = 3. C) Overall lysine (Kac), tubulin and histone acetylation as determined by immunoblot analysis of lysates from parental 293 cells incubated in the presence or absence of the NamPT inhibitor FK866 (2 μM). Results shown are representative of three independent repetitions. D) Overall lysine (Kac), tubulin and histone acetylation as determined by immunoblot analysis of lysates from parental 293 cells and stably transfected PARP1cd cell lines. Expression of the fusion proteins was confirmed by detection of the EGFP tags, while α-tubulin served as a loading control. Results shown are representative of three independent repetitions. E) Mitochondrial lysine acetylation (Kac) as determined by immunoblot analysis of mitochondrial extracts from parental 293 cells and stably transfected PARP1cd cell lines. The mitochondrial protein apoptosis-inducing factor (AIF) served as a loading control. Results shown are representative of three independent repetitions. mP - 293mitoPARP1cd, pP – 293pexPARP1cd, cP – 293cytoPARP1cd, erP – 293erPARP1cd.

Figure 3

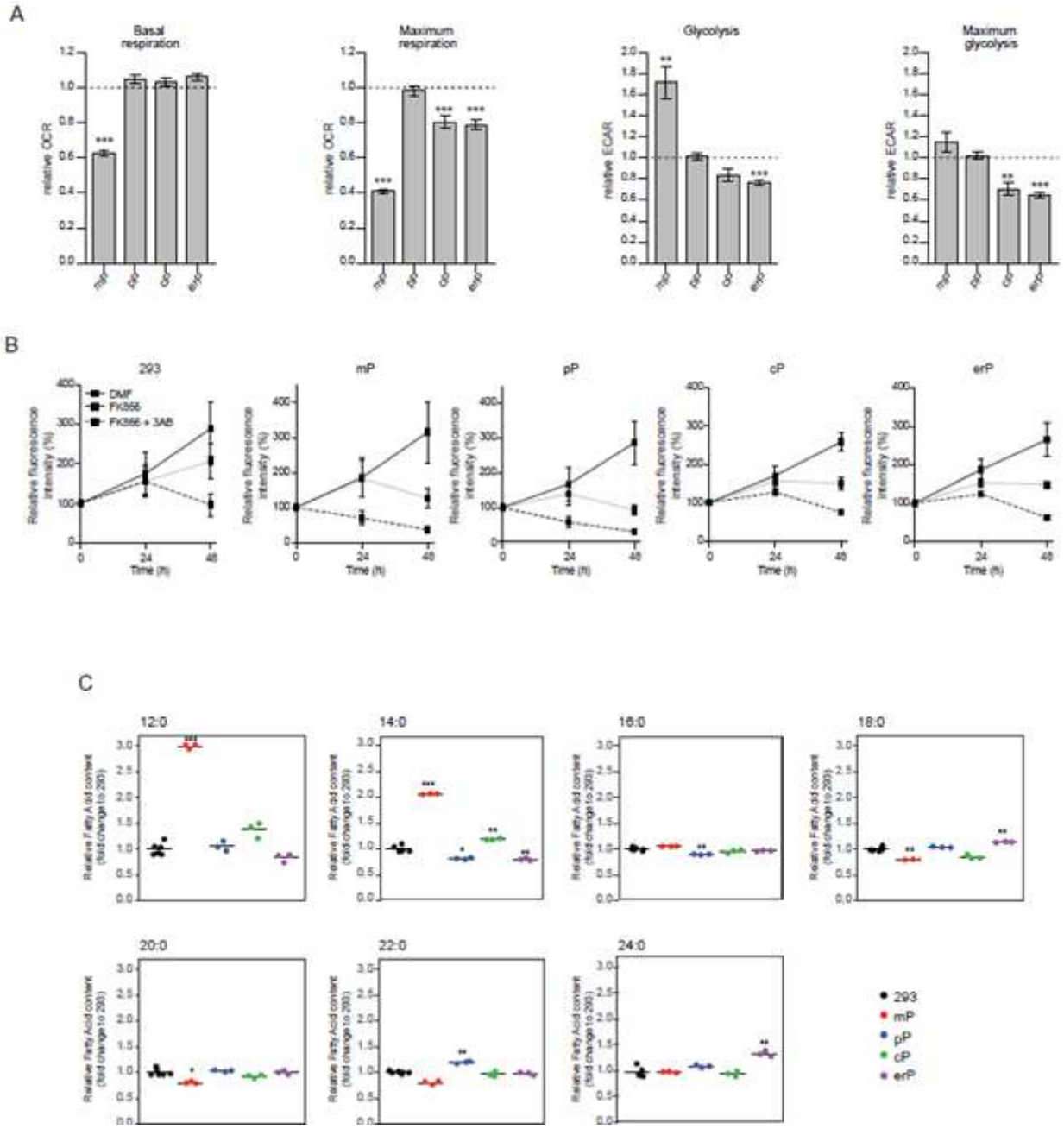

Figure 3

Direct mitochondrial NAD+ depletion affects bioenergetics A) Activity and integrity of mitochondrial respiration in terms of oxygen consumption rate (OCR), and glycolysis in terms of extracellular acidification rate (ECAR) in stably transfected PARP1cd cell lines compared to parental 293 cells as determined by extracellular flux analysis. Data are presented relative to parental 293 cells as mean ± SEM where n = 3. *p ≤ 0.05, **p ≤ 0.01, ***p ≤ 0.001 (Student's t-test). B) Activity of mitochondrial NAD-dependent dehydrogenases as measured by resazurin assay in parental 293 cells and stably transfected PARP1cd cell lines in the absence or presence of the NamPT inhibitor FK866 (2 μM) or its solvent DMF. Additionally, cells were incubated in the presence of both FK866 (2 μM) and the PARP inhibitor 3-aminobenzamide (3AB, 1 mM). Data are presented as mean ± SD where n = 3. C) Relative cellular abundance of fully saturated fatty acids in stably transfected PARP1cd cell lines compared to parental 293 cells as determined by gas chromatography. The abundance of each fatty acid is normalized to total fatty acid content. D) Data are presented as mean ± SD where n ≥ 3. *p ≤ 0.05, **p ≤ 0.01, ***p ≤ 0.001 (Student's t-test). mP - 293mitoPARP1cd, pP – 293pexPARP1cd, cP – 293cytoPARP1cd, erP – 293erPARP1cd.

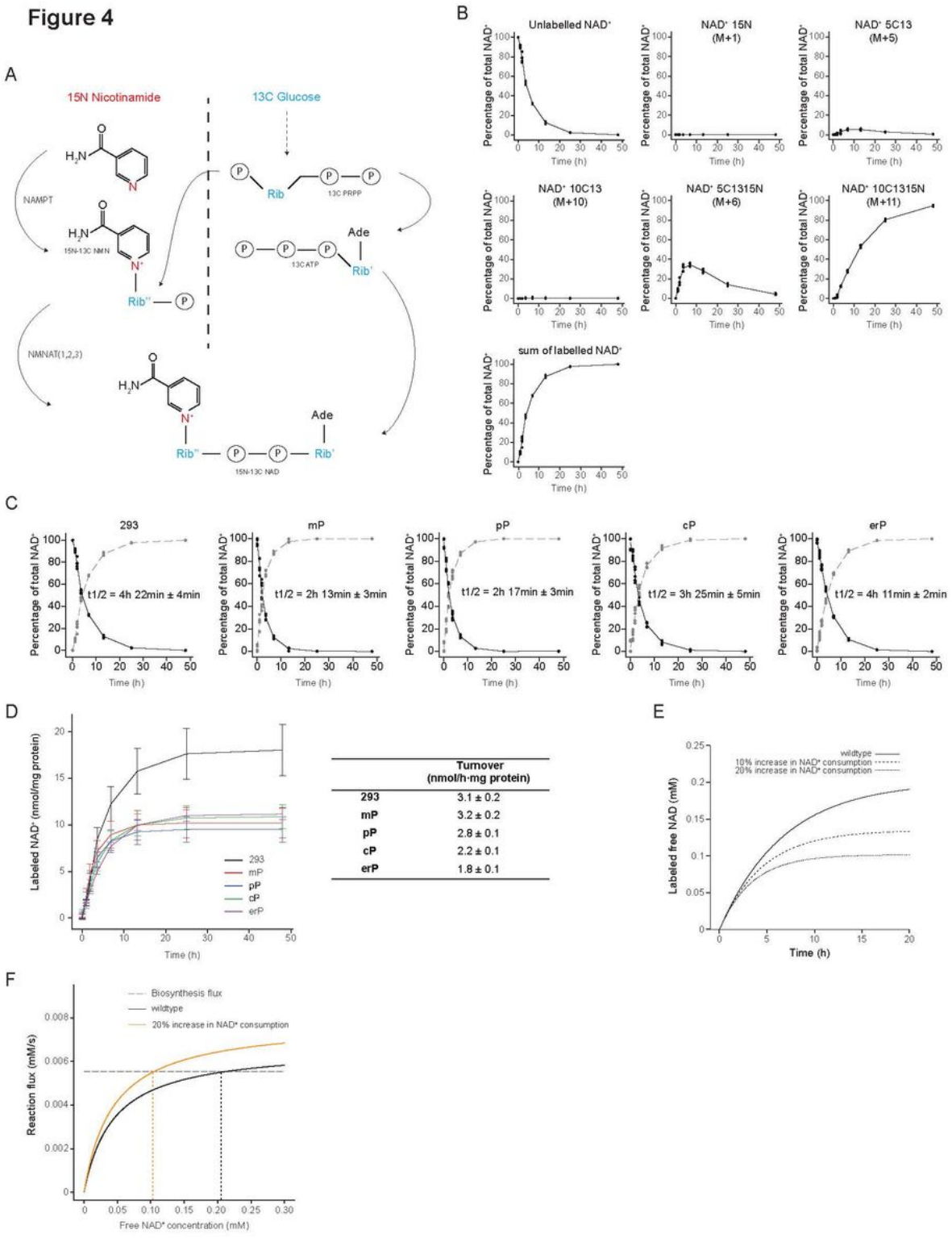

Figure 4

Total cellular NAD+ turnover is not increased by PARP1cd overexpression A) Schematic representation of the labelling approach used in this study. Cells were incubated with isotopically labelled nicotinamide (15N, red) or glucose (13C, blue), allowing for labelling on both the Nam-moiety and the ribose-moieties. B) The time-dependent appearance of labelled isotopologs is accompanied by the disappearance of unlabeled NAD+ upon incubation of parental 293 cells in the presence of isotopically labelled

nicotinamide (15N), and glucose (13C) where n = 6. C) Half-life of NAD+ in parental 293 and PARP1cd cell lines in terms of the timedependent appearance of the sum of labelled NAD+ species (dashed line) and respective disappearance of unlabeled NAD+ (solid line) where n = 6. D) Time courses for NAD+ labelling in parental 293 and PARP1cd cell lines normalized to steady state NAD+ concentrations per protein. Data are presented as means ± SD where n ≥ 6. The table lists the estimated NAD turnover. E) Simulations of NAD+ labelling time courses using a minimal mathematical model of NAD+ biosynthesis and consumption. PARP1cd overexpression was modelled by increasing the maximal velocity of NAD+ consumption while keeping the maximal velocity of NAD+ biosynthesis constant. F) Demand-supply model showing the dynamics of NAD+-consumption and NAD+- biosynthesis in isolated enzymes. To achieve steady state both processes have to balance each other. The intersection therefore represents the theoretical steady state concentration of NAD, demonstrating the kinetic balancing effect that leads to decreased NAD concentration upon overexpression of PARP1cd. mP - 293mitoPARP1cd, pP – 293pexPARP1cd, cP – 293cytoPARP1cd, erP – 293erPARP1cd

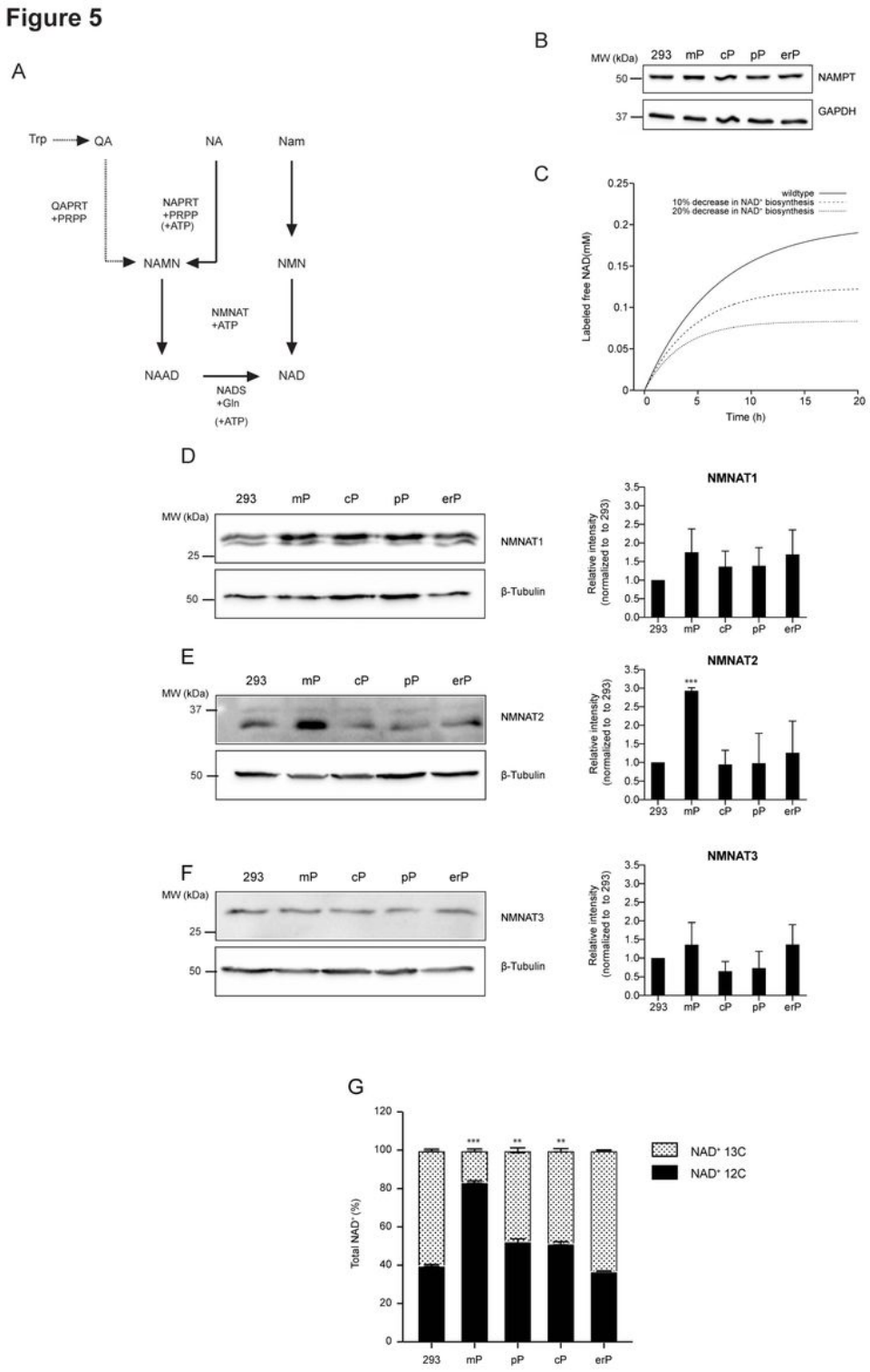

Figure 5

Stable NAD+ biosynthesis kinetically limits NAD+ consumption A) Schematic representation of the de novo, Preiss-handler and salvage NAD biosynthetic pathways. B) NamPT Immunoblot analysis of lysates from parental 293 cells and stably transfected PARP cell lines. GAPDH served as a loading control. Results shown are representative of four repetitions. C) Simulations of NAD+ labelling time courses using a minimal mathematical model of NAD+ biosynthesis and consumption, demonstrating the effect of

NAD+ biosynthesis decrease while keeping the maximal velocity of NAD+ consumption constant D) NMNAT1 protein expression in PARP1cd cell lines compared to parental 293 cells as analyzed by western blotting. β -tubulin served as a loading control. Data are presented as mean ± SD where n = 4. E) NMNAT2 protein expression in PARP1cd cell lines compared to parental 293 cells as analyzed by western blotting. β -tubulin served as a loading control. Data are presented as mean ± SD where n = 4. *p ≤ 0.05, **p ≤ 0.01, ***p ≤ 0.001 (Student's t-test). F) NMNAT3 protein expression in PARP1cd cell lines compared to parental 293 cells as analyzed by western blotting. β -tubulin served as a loading control. Data are presented as mean ± SD where n = 4. G) Distribution of NAD labeling following 48 h incubation of parental 293 cells and stably transfected PARP1cd cell lines in the presence of NA 13C. mP - 293mitoPARP1cd, pP – 293pexPARP1cd, cP – 293cytoPARP1cd, erP – 293erPARP1cd

Figure 6

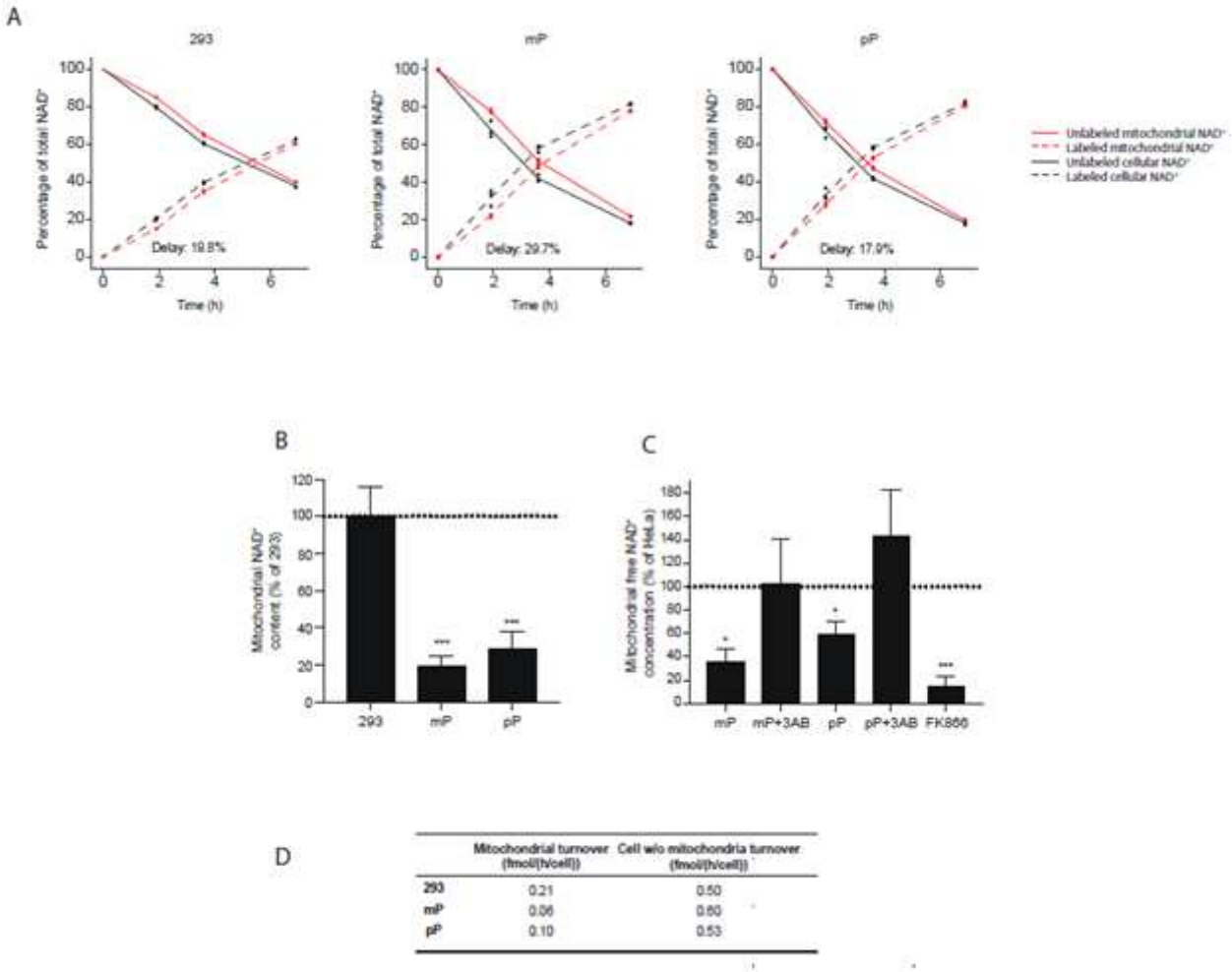

	Mitochondrial turnover (fmol/[h/cell])	Cell w/o mitochondria turnover (fmol/[h/cell])
293	0.21	0.50
mP	0.06	0.60
pP	0.10	0.53

Figure 6

Direct, but not indirect depletion of mitochondrial NAD+ is detrimental to cellular homeostasis A) Time-dependent appearance of the sum of labelled NAD+ species (dashed line) and disappearance of unlabeled NAD+ (solid line) in whole cell lysate (WCL, black) and mitochondria (red) upon incubation in the presence of 15N nicotinamide and 13C glucose. Delays are presented as the difference between

mitochondrial and extramitochondrial (total minus mitochondrial) half-lives relative to the half-life of extramitochondrial NAD+. Experimental data where n ≥ 3. mP - 293mitoPARP1cd, pP – 293pexPARP1cd. B) Mitochondrial NAD+ content in parental 293 cells and stably transfected 293mitoPARP1cd (mP) and 293 pexPARP1cd (pP) cell lines as determined by mitochondrial isolation followed by methanol extraction and LC-MS analysis. Results were normalized to protein content and data are represented relative to parental 293 cells as mean ± SD where n = 3. *p ≤ 0.05, **p ≤ 0.01, ***p ≤ 0.001 (Student's ttest). C) Free mitochondrial NAD+ concentration in untreated HeLa cells, as well as upon transient transfection with red mitoPARP1cd (mP) and pexPARP1cd (pP) constructs. NAD+ concentrations were calculated from sensor (488/405 nm)/control (488/405 nm) fluorescence ratios determined by flow cytometry (see Figure S6). Measurements were performed in presence or absence of 3-aminobenzamide (3AB, 1 mM, 48h), and incubation of HeLa cells with FK866 (2 μM) served as a positive control. Results are represented relative to untransfected control cells as mean ± SD where n ≥3. D) The mitochondrial and cytosolic NAD+ turnover per cell as calculated for parental 293 cells, as well as stably transfected transfected 293mitoPARP1cd (mP) and 293 pexPARP1cd (pP) cell lines taking into account the cellular NAD+ distribution.

Figure 7

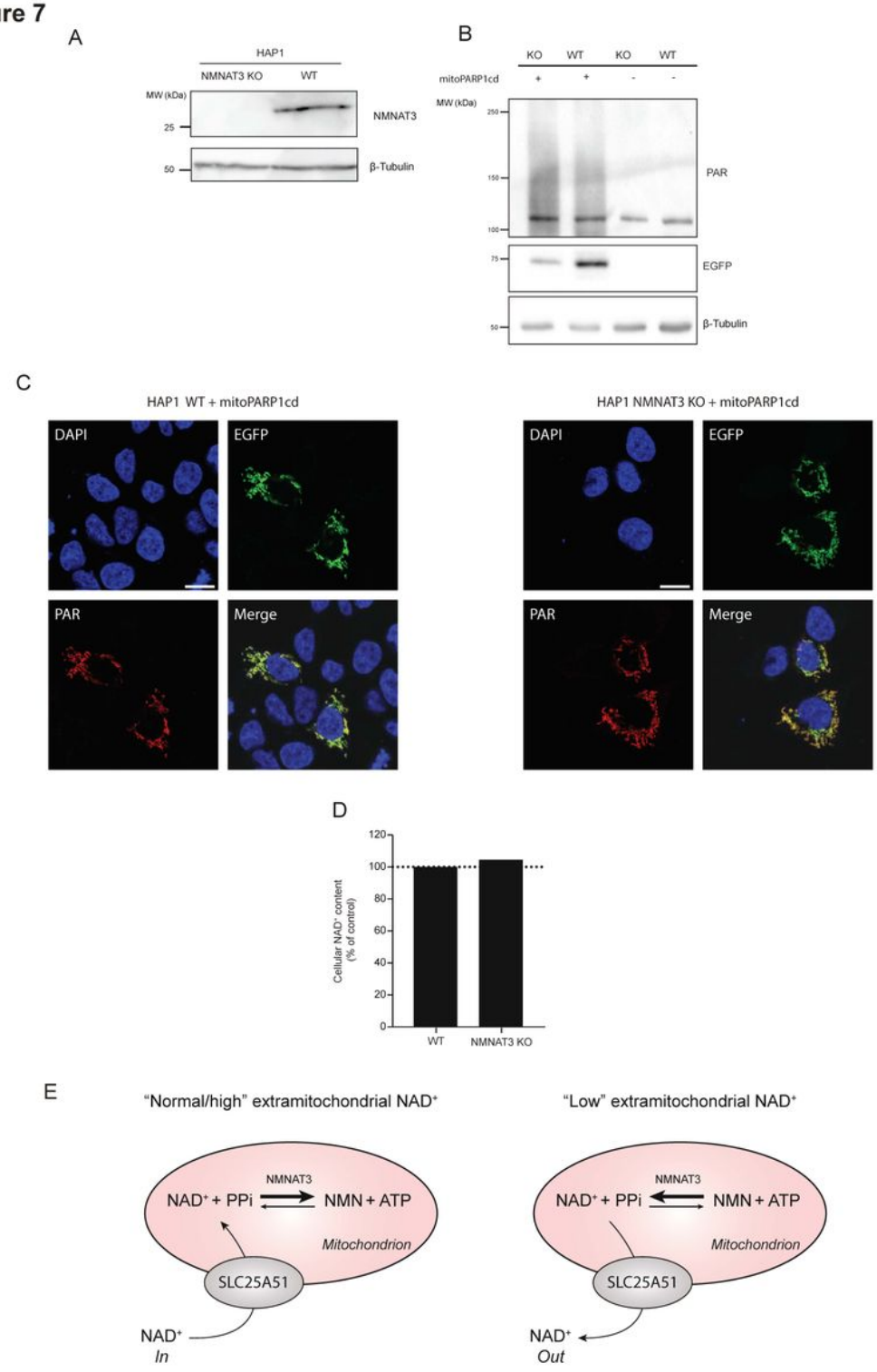

Figure 7

Supplementary Files

This is a list of supplementary files associated with this preprint. Click to download.

- NADpoolsSupplementaryinformationcompressed.pdf